Towards a background-free neutrinoless double beta decay experiment based on a fluorescent bicolor sensor

Iván Rivilla,[a] Borja Aparicio,[b] Juan M. Bueno,[c] David Casanova,[a,d] Claire Tonnelé,[a] Zoraida Freixa,[d,e] Pablo Herrero,[a] Celia Rogero,[f,a] José I. Miranda,[g] Rosa M. Martínez-Ojeda,[c] Francesc Monrabal,[a,d] Beñat Olave,[g] Thomas Schäfer,[h,d] Pablo Artal,[c] David Nygren,[j] Fernando P. Cossío,[a,b,1] Juan J. Gómez-Cadenas[a,d,1]

[a] *Donostia International Physics Center (DIPC), Manuel Lardizabal Ibilbidea 4, 20018 San Sebastián / Donostia, Spain*

[b] *Department of Organic Chemistry I, University of the Basque Country (UPV/EHU), Centro de Innovación en Química Avanzada (ORFEO-CINQA), Manuel Lardizabal Ibilbidea 3, 20018 San Sebastián / Donostia, Spain*

[c] *Laboratorio de Óptica (LOUM) & Centro de Investigación en Óptica y Nanofísica (CiOyN), University of Murcia, Espinardo Campus, 30100 Murcia, Spain*

[d] *Ikerbasque, Basque Foundation for Science, María Díaz de Haro 3, 6, 48013 Bilbao, Spain*

[e] *Department of Applied Chemistry, Faculty of Chemistry, University of the Basque Country (UPV-EHU), San Sebastián / Donostia, Spain*

[f] *Materials Physics Center CFM (CSIC-UPV/EHU), Manuel Lardizabal Ibilbidea 5, 20018 San Sebastián / Donostia, Spain*

[g] *SGIker NMR Facility, University of the Basque Country (UPV/EHU), Avda. Tolosa 72, E-20018 San Sebastián / Donostia, Spain*

[h] *NanoBioSeparations Group, POLYMAT, University of the Basque Country (UPV/EHU), Avda. Tolosa 72, E-20018 Donostia/San Sebastián, Spain*

[i] *Department of Physics, University of Texas at Arlington, Arlington, TX 76019, USA*

E-mail: jjgomezcadenas@dipc.org, fp.cossio@ehu.es

[1] corresponding author

Abstract: Observation of the neutrinoless double beta decay ($\beta\beta0\nu$) mode is the only practical way to establish that neutrinos are their own antiparticles. Due to the smallness of neutrino masses, the lifetime of $\beta\beta0\nu$ is expected to be at least ten orders of magnitude larger than the backgrounds from the natural radioactive chains that can mimick the experimental $\beta\beta0\nu$ signature. The most robust identification of $\beta\beta0\nu$ decays requires the definition of a signature that radioactive backgrounds cannot generate. Together with excellent energy resolution, this signal could be the observation of the daughter atom in the decay, since no known background processes directly induce a Z+2 transformation. In particular, the $\beta\beta0\nu$ decay of ^{136}Xe could be established by detecting the daughter atom, $^{136}Ba^{2+}$ in its doubly ionised state. Such a detection could be achieved via a sensor made of a monolayer of fluorescent molecular indicators. The Ba^{2+} dication would be captured by one of the molecules in the sensor, and the presence of a single chelated indicator would be subsequently revealed by a strong fluorescent response from repeated interrogation with a laser system. We demonstrate a significant step towards a "barium-tagging" experiment, based on a new fluorescent bicolor indicator which we propose as the core of a sensor able to detect single Ba^{2+} ions in a high-pressure xenon gas detector.

Keywords: neutrinoless double beta decay ; fluorescent molecular indicator ; barium tagging ; wide field two photon absorption microscopy.

1 Main

Double beta decay ($\beta\beta$) is a very rare nuclear transition in which a nucleus with Z protons decays into a nucleus with $Z + 2$ protons and the same mass number A. The decay can occur only if the initial nucleus is less bound than the final nucleus, and both bound more than the intermediate $Z + 1$ nucleus. Two decay modes are usually considered [1]:

• The standard two-neutrino mode ($\beta\beta2\nu$), consisting in two simultaneous beta decays, $(Z, A) \rightarrow (Z + 2, A) + 2\, e^- + 2\, \overline{\nu}_e$, which has been observed in several isotopes with typical half-lives in the range of 10^{18}–10^{21} years.

• The neutrinoless mode ($\beta\beta0\nu$), $(Z, A) \rightarrow (Z + 2, A) + 2\, e^-$, which violates lepton-number conservation and can occur if and only if neutrinos are Majorana particles [2], particles that are identical to their antiparticles. An unambiguous observation of such decay would have deep implications in particle physics and cosmology, offering a mechanism for leptogenesis [3] and a potential explanation for the cosmic asymmetry between matter and antimatter [4]. Furthermore, Majorana neutrinos could provide an explanation of the smallness of the neutrino masses compared with that of the other leptons, through the so-called see-saw mechanism [5–7].

Double beta decay ($\beta\beta$) experiments have been searching $\beta\beta0\nu$ in several isotopes for more than half a century without finding clear evidence of a signal. The current best lower limit on the lifetime ($T^{0\nu}_{1/2}$) of $\beta\beta0\nu$ processes has been obtained for the isotope ^{136}Xe, for which $T^{0\nu}_{1/2} > 10^{26}$ yr [8]. Two other isotopes, ^{76}Ge and ^{128}Te, have also been studied with similar sensitivities, yielding no evidence for bbonu decay [9, 10]. A new generation of $\beta\beta0\nu$ experiments will aim to improve the sensitivity to $T^{0\nu}_{1/2}$ by several orders of magnitude [11]. These searches will require very large exposures, measured in ton-years, but even more importantly, a greatly enhanced capability to suppress backgrounds from false events.

The most obvious background to $\beta\beta0\nu$ is the $\beta\beta2\nu$ decay, which also produces two electrons and the same daughter atom as in the neutrinoless mode, while having a much faster decay rate. Near the end point energy (Q), however, the $\beta\beta2\nu$ process is very strongly suppressed by kinematics and its contamination to the $\beta\beta0\nu$ signal turns out to be negligible for a detector with good energy resolution, as discussed in detail in Methods.

Instead, due to the irreducible presence of trace amounts of the radioactive decay chains of ^{238}U and ^{232}Th in materials of the detector, their false signatures need to be suppressed by a very large factor. The decay of other radioactive isotopes created by neutron activation are also a concern. All $\beta\beta$ experiments are built with ultra-pure materials, operate in underground laboratories (to mitigate the impact of cosmic rays) and are protected by massive, ultra-pure shields. These strategies reduce the ambient background by many orders of magnitude, but putative $\beta\beta0\nu$ events must still be extracted against tens of millions of spurious interactions.

The most powerful discriminant against backgrounds other than $\beta\beta2\nu$ would be the detection of the daughter atom, which is displaced two steps higher in the periodic table relative to its parent. In particular, the decay $^{136}\mathrm{Xe} \rightarrow \mathrm{Ba} + 2\,\mathrm{e}\,(+2\,\overline{\nu}_\mathrm{e})$, will create a Ba^{2+} dication as the most likely outcome in xenon gas. In pure xenon gas, no known radioactive process will produce the appearance of such ion, *in coincidence with two electrons*. The implementation of a robust Ba^{2+} detection technique would facilitate the positive observation of $\beta\beta0\nu$.

The possibility of barium tagging in a xenon time projection chamber (TPC) was proposed in 1991 by Moe [12], and has been extensively investigated for the last two decades [13–15]. Recently the nEXO collaboration has demonstrated the imaging and counting of individual barium atoms in solid xenon by scanning a focused laser across a solid xenon matrix deposited on a sapphire window [16]. This is a promising step for barium tagging in liquid xenon. The technique originally proposed by Moe and being pursued by nEXO relies on Ba^{+} fluorescence imaging using two atomic excitation levels in very low density gas. In liquid xenon, recombination is frequent and the barium daughters are distributed across charge states from 0 to 2+ [17], with sizeable populations of neutral Ba and Ba^{+}. In the high pressure gas phase, however, the initially highly ionized barium daughter quickly captures electrons from neutral xenon, stopping at Ba^{2+} beyond which recombination is minimal [18].

A molecule whose response to optical stimulation changes when it forms a supramolecular complex with a specific ion is a fluorescent indicator, and ions thus bound to molecules are generally referred to as being chelated (one also refers to molecules having formed a complex with the ion as "chelated molecules"). In 2015, Nygren proposed a Ba^{2+} sensor based on fluorescent molecular indicators that could be incorporated within a high-pressure gas xenon TPC (HPXe) [19], such as those being developed by the NEXT Collaboration [11, 20–22]. The concept was further developed in [23] and followed by an initial proof of concept [24] which resolved individual Ba^{2+} ions on a thin quartz plate with Fluo-3 (a common indicator in biochemistry) suspended in polyvinyl alcohol (PVA) to immobilise the molecular complex and facilitate optical imaging. The experiment demonstrated, with 2nm rms super-resolution, single-ion sensitivity confirmed by single-step photobleaching; this work constituted an essential first step toward barium tagging in a HPXe.

However, an experiment aiming to detect Ba^{2+} in a HPXe, requires a sensor which differs substantially from that used in [24]. First, the surface density of indicators in the sensor needs to be high, in order to ensure maximum ion capture efficiency. Second, the indicators must be able

to form a supramolecular complex with Ba^{2+} in dry medium — the Gibbs energy of the process in xenon gas must be negative. Third, the indicators must respond to optical stimulation with a very distinctive signal that allows unambiguous identification of the molecule that has chelated the single ion produced in the $\beta\beta0\nu$ decay and good discrimination from the background due to the uncomplexed molecules in the surroundings. In other words, a discrimination factor, F, between the response (in dry medium) of the chelated indicator and the residual response of unchelated molecules must be large. A significant step in developing dry sensors was carried out in [25], where molecular compounds based on aza-crown ethers and using conventional fluoropohores such as pyrene [26, 27] and anthracene [28] were studied, although the discrimination factors were not quantified in that work. Indeed, to our knowledge, F has not yet been measured for a dry sensor.

In this paper we demonstrate a significant step towards a barium-tagging experiment in a HPXe, based on a new fluorescent bicolor indicator (FBI) which we propose as the core of a sensor able to detect single Ba^{2+} ions in a high-pressure gas detector. The indicator is synthesised to bind strongly to Ba^{2+} and to shine very brightly when complexed with Ba^{2+}. Furthermore, the emission spectrum of the chelated indicators is significantly blue-shifted with respect to the unchelated species, allowing an additional discrimination of almost two orders of magnitude. Using silica as a physical substrate, we demonstrate that:

• FBI boasts a very large discrimination factor in dry medium (silica-air), $F = (25 \pm 6) \times 10^4$, to our konwledge the largest found in the literature.

• The indicator efficiently chelates Ba^{2+} in dry medium (silica-vacuum). This was proved sublimating barium perchlorate ($Ba(ClO_4)_2$) on FBI molecules deposited on a silica pellet and interrogating the indicators using two photon absorption (TPA) microscopy. To our knowledge this is the first time that the formation of a Ba^{2+} supramolecular complex in dry medium is demonstrated.

Furthermore, we have performed density functional theory (DFT) calculations which show that our experimental result is consistent with the exergonic nature of the binding of $Ba(ClO_4)_2$ to FBI in vacuum. Extension of those calculations to the gas phase show that binding of Ba^{2+} to FBI is much more exergonic than binding of $Ba(ClO_4)_2$ to FBI in vacuum, and for all solvation states of Ba^{2+} in xenon and all relevant pressures. Furthermore, the process converges spontaneously when the system FBI·Ba^{2+} is started at distances of around 1 nm. From these calculations one can conclude that the formation of supramolecular complexes observed in vacuum imply that FBI indicators can chelate Ba^{2+} ions with high efficiency (using a dense layer of indicators) in an HPXe experiment. We further show that the large value of F found for FBI allows the unambiguous identification —using TPA microscopy— of a single chelated indicator, even when indicator density is high.

2 Design and synthesis of FBI compounds

Our criteria to design FBIs are summarised in Figure 1. The indicator includes, as essential components, a metal binding group (a convenient moiety is a coronand formed by a N-aryl-aza-crown ether [29, 30]) and a fluorophore, in line with previously developed designs for fluorescent sensors capable to capture metal cations in solution [31]. Figure 1a shows the expected behaviour of a fluorescent monocolor indicator (FMI), in which the fluorophore does not modify substantially its π-molecular orbital structure. In these hydrocarbon or heterocyclic scaffolds, an electron donating group (EDG) close to the fluorophore (for instance, an amino group of the aza-crown ether) can

promote a photoinduced electron transfer (PET) that quenches the fluorescence in the absence of a binding cation. In contrast, sensor-cation complexation results in an OFF-ON enhancement of the photoemission intensity [32] with $\Delta\lambda \approx 0$ (Figure 1a). As a consequence, in general only changes in the intensity of the emitted fluorescent signal upon Ba^{2+}complexation should be observed under this PET mechanism. In addition, this kind of sensors has been used in aqueous solution for metals of biological interest [33] and mainly for the capture of cations such as K^+ by using bicylic aza-cryptads [34]. Figure 1b illustrates the desired behaviour of a FBI indicator upon binding to Ba^{2+} ions. A convenient way to generate this kind of sensors with $\Delta\lambda \neq 0$ consists of generating an intramolecular photoinduced charge transfer (PCT) by modifying the response of an EDG with the rest of the fluorophore [31]. Upon coordination with the cation, the change in the dipole moment of the supramolecular entity can generate a Stokes shift. However, in general these PCT phenomena promote only slight blue-shifts [35] and depend on the polarity of the environment, thus being strongly affected by solvent effects. Actually, most PCT sensors work in water and bind cations such as Na^+ and K^+ by means of bicyclic aza-cryptands [36, 37], among other groups like acidic chelators or podands. Therefore, the design and chemical synthesis of efficient FBIs with large enough $\Delta\lambda$ values in the gas phase still constitutes an important challenge.

Within this context, we require that: **a**, the chelating group binds the cation with a high binding constant; **b**, the indicator response in dry medium is preserved and preferably enhanced w.r.t. the response in solution, and **c**, the fluorophore exhibits distinct response in the visible region for the chelated and unchelated states (thus the term bicolor indicator). To that end, the synthesis of FBI compounds incorporates a custom-designed fluorophore possessing two aromatic components denoted as Ar^1 and Ar^2 in Figure 1b that are connected by a free-rotating σ bond. The main fluorophore component Ar^1 consists of a nitrogen-containing aromatic polyheterocycle [38–41] that can bind the Ba^{2+}cation, thus modifying its electronic structure and decoupling this moiety from Ar^2, which in turn can generate a π-cation interaction [42] (Figure 1b). The expected shift in response to coordination should provide a strong signature of a bound indicator, which exhibits a blue shift, over a background of unbound species. Furthermore we require that the indicator response does not form supra-molecular complexes with light elements in the barium column of alkaline-earth elements (e.g, beryllium, calcium and magnesium) as well as with other close alkaline ions common in the environment such as Na^+ and K^+.

The chemical synthesis of our sensors is shown in Figure 1c. The process starts with the double addition-elimination reaction between 2-aminopyridines (X=CH) **1a-c** or 2-aminopyrimidine **1b** (X=N) and 2,4-dibromoacetophenone **2**. Bicyclic heterocycles **3a-c** reacted with aza-crown ethers **4a-c** in the presence of a Pd(0)/DavePhos catalytic system to generate intermediates **5a-e** in moderate (30%) to very good (95%) yields. Finally, these latter adducts were coupled with aromatic 1,2-dibromides **6a,b** by means of a catalytic system formed by a Pd(II) salt and XPhos to yield the desired FBI compounds **7aa-cb**. In this latter step, the formal (8+2) reactions were carried out in the presence of potassium carbonate or cesium carbonate (compound **7ec**) as weak bases.

Finally, we performed experiments to determine the photo-physical properties of compounds **7**. The results of these experiments, which are described in the Method section, allowed us to select compound **7ca** as the optimal combination of structural and electronic features to fulfil our design criteria. We refer henceforth to compound **7ca** as FBI.

3 Discrimination factor

To demonstrate the performance as Ba^{2+} sensor of our bicolor indicator, we adopted silica gel as a solid phase support. Adsorption of the molecule on the silica surface permits the exposure of at least one side of its crown ether moiety to the interaction with Ba^{2+} cations. In addition, this solid-gas interface topology preserves the conformational freedom required to reach the coordination pattern observed in our calculations(see Methods for further information). Therefore, the emission spectrum recorded on silica for the coordinated indicator keeps the essential features of our design, in particular the colour shift.

Two samples were manufactured. Sample SF was prepared depositing 2.3×10^{-5} mmol of FBI (from an CH_3CN solution) on a silica pellet. Sample SBF was formed depositing 7.4×10^{-8} mmol of FBI/acetonitrile solution on a silica pellet saturated with barium perchlorate. The optimal concentration of barium salt was determined by a titration experiment, described in the Methods section. The ratio between the concentrations of SF and SBF was $C_r = 310 \pm 6$, where the 2% relative error was found propagating the uncertainties in the measurements of the volumes of the solutions. Figure 2a shows the emission spectrum of the SF (SBF) samples for an excitation light of 250 nm, recorded by a fluorimeter after evaporating the solvent and subtracting the background signal due to the silica (see Methods for a discussion).

A robust separation between both SF and SBF can be achieved selecting a blue-shifted wavelength range, $\lambda_f = (\lambda_{min}, \lambda_{max})$, through a band filter. Call $C(\lambda)$ the emission spectrum of chelated molecules (*e.g.*, the blue curve in Figure 2a) and $U(\lambda)$ that of the unchelated molecules (green curve in Figure 2a). The fraction of $C(\lambda)$ selected by the filter is $f_c = c/C$, where $c = \int_{\lambda_{min}}^{\lambda_{max}} C(\lambda)d\lambda$ and $C = \int C(\lambda)d\lambda$. Analogously, the fraction of $U(\lambda)$ selected by the filter is $f_u = u/U$, with $u = \int_{\lambda_{min}}^{\lambda_{max}} U(\lambda)d\lambda$ and $U = \int U(\lambda)d\lambda$. Defining $D_r = f_c/f_u$, the discrimination factor is simply:

$$F = D_r \cdot C_r \tag{3.1}$$

For this study we chose a band filter λ_f =(400 – 425) nm, corresponding to the region shaded in blue in Figure 2a. A larger separation could be obtained including smaller wavelengths (*e.g.*, selecting $\lambda_f < 400$ nm), but the fluctuations associated to the subtraction of the baseline and the rapid variation of $C(\lambda)$ would result also in large uncertainties. We find $f_c = 0.29 \pm 0.03$, $f_u = 0.0036 \pm 0.0007$, and $D_r = 80 \pm 18$. The ~20% relative error in the estimation of f_u is dominated by the subtraction of the baseline, while the ~10% relative error in the estimation of f_c is found by varying the range of the filter by ± 1 nm. Using equation 3.1 we find $F = (2.5 \pm 0.6) \times 10^4$.

4 A proof of concept of chelation in dry medium

An important step towards the detection of Ba^{2+} HPXe-TPCs, is the demonstration that the ions can be chelated in the absence of a solvent. This requires exposing a sample of FBI molecules deposited in a solid-vacuum interface, to a source of Ba^{2+} ions.

To achieve this goal, we designed a sublimation experiment as follows. We started by compressing silica powder to form thin silica pellets, then we deposited a FBI/CH_3CN solution on them and evaporated the solvent. Two similar SFp pellets (SFpA and SFpB) were prepared

depositing 7.4×10^{-8} mmol of indicator per mg of silica, equivalent to 1.3×10^{15} molecules of FBI. SFpA was kept as reference for unchelated molecules and SFpB was introduced in an ultra-high vacuum chamber (Figure 3a) where barium perchlorate was sublimated. Sublimation was performed using a Kudsen cell at a temperature around 700 K. The evaporation rate was continuously monitored in-situ with a micro-balance. The total thickness of $Ba(ClO_4)_2$ deposited was 10 Å, equivalent to a layer of 7.6×10^{14} molecules. Figures 3b and 3c display images of the pellet before and after sublimation under an excitation light of 365 nm. The blue shift after sublimation is clearly visible even to the naked eye, showing that a large number of indicators in the pellet's surface were chelated.

The next step was to scan both SFpA and SFpB pellets in our two-photon absorption (TPA) microscopy setup [43], described with some detail in the Methods section. We performed tomographies (*e.g.*, Z-X scans) using two filters: a high pass "green" filter, $\lambda > 450$ nm, and a band pass "deep blue" filter, (400 – 425) nm. The Z-X scans were performed with infrared light (800 nm) and at a nominal laser power of 100 mW. In addition, we performed 3D tomographies, which were assembled from 40 XY scans of 75 $\mu m^2 \times 75\ \mu m^2$. Each scan corresponded to a different depth of Z, in steps of 10 µm. The resulting images were then combined in a 3D image using custom software [44].

Our results are summarised in Figure 2. We started by measuring the control pellet, SFpA. The Z-X tomography acquired using the green filter (Figure 2c), reveals a region of about 20 µm in depth that corresponds to the area of the pellet where FBI molecules were immobilised. Since they are unchelated molecules they are visible with this filter but not with the deep blue filter (Figure 2b). Instead, for SFpB, the green profile (Figure 2e) is similar to the one measured for SFpA, but the deep blue tomography (Figure 2d), shows a clear signal in the same 20 µm region around the pellet surface. This can exclusively be ascribed to the emission of chelated molecules, therefore demonstrating that the sublimation deposited the Ba^{2+} rather uniformly, resulting in a layer of chelated molecules. Finally, Figure 2f shows green and deep blue 3D tomographies confirming that the spatial distribution of the chelated molecules follows that of the unchelated indicators.

Density Functional Theory (DFT) calculations (described with detail in Methods) show that the Gibbs energy associated with binding of $Ba(ClO_4)_2$ to FBI is −80.0 kcal/mol, confirming that the process is very exergonic, as expected given the experimental result described above and fully compatible with the high binding constant found for this process.

5 Chelation of Ba^{2+} by FBI indicators in xenon gas

In a HPXe experiment, the Ba^{2+} created in the $\beta\beta0\nu$ decay will slowly drift to the cathode (with a drift velocity of about 220 cm s^{-1}) picking up neutral xenon atoms on its way and in a variety of solvation states, $[BaXe_N]^{2+}$ (with $N = 1, 2...$) will be formed [45]. At the large pressures typical of a HPXe (∼ 20 bar), it has been estimated that $N \sim 8$.

What is the relevance of the proof of concept described above (which demonstrates the observation of the reaction $Ba(ClO_4)_2$·FBI in vacuo), for a HPXe experiment, which requires that the reaction $[BaXe_N]^{2+}$·FBI occurs efficiently in high pressure xenon? Density functional theory (DFT) can shed light on this question. Our calculations show that the interaction between a $Ba{\cdot}Xe_8^{2+}$ cluster and FBI results in a very exergonic process with a Gibbs reaction energy of −195.9 kcal/mol, almost as large as the Gibbs energy associated to the interaction of a naked dication with the indicator

(−197.5 kcal/mol) and much larger than the energy associated with binding of $Ba(ClO_4)_2$ with FBI (−80.0 kcal/mol). Furthermore, we find that the Gibbs energy of the FBI·Ba^{2+} changes very little in the range between 1 and 30 bar (see Table 3 in the Extended Data section).

Furthermore, our calculations suggest that a layer of indicators with a density of about 1 molecule per squared nanometer will efficiently chelate Ba^{2+}. Figure 4 shows the computed structures of FBI and a $Ba^{2+}Xe_8$ cluster at different $N\cdots Ba^{2+}$ distances. When optimisation of **7ca**–$Ba^{2+}Xe_8$ pair was started at a $N\cdots Ba^{2+}$ separation of 8 Å, the cluster spontaneously converged to a local minimum in which the original Xe_8 structure was squeezed around the convex face of FBI and the $N\cdots Ba^{2+}$ distance was 3.27 Å. From this intermediate state the whole cluster converged to the chelated species, in which the $N\cdots Ba^{2+}$ distance was found to be 2.9 Å. This latter energy minimum was calculated to be ca. 107 kcal/mol more stable than the previous intermediate state. In addition, the geometric parameters of the minimum energy cluster —in which the eight Xe atoms are distributed around FBI— are very similar to those found for FBI·Ba^{2+} and FBI·$Ba(ClO_4)_2$ complexes.

6 Discussion: towards a sensor for Ba^{2+} tagging

In addition of a sensor capable of chelating with high efficiency Ba^{2+}, a future HPXe experiment with barium tagging needs to be able to distinguish unambiguously the signal of a single complexed indicator from the background of unchelated surrounding molecules. Here we show that the large discrimination factor of FBI permits such a robust observation of single chelated molecules even for densely packed sensors.

Consider a TPA microscopy system similar to the one used in this work, but with optimised parameters, *e.g.*, a 800 nm pulsed laser, with a repetition rate (f) of 100 MHz, pulse width (τ) of 100 fs FWHM and moderately large numerical aperture, $NA = 0.95$. Following [46], we take the overall light collection efficiency of the system to be $\epsilon_c = 10\%$. Focusing the laser in a diffraction-limited spot (a circle of ~ 0.5 µm diameter) results in a photon density of 1.7×10^{31} photons/pulse/cm^2/W.

Assume now that a single FBI molecule complexed with a Ba^{2+} ion and m unchelated indicators are contained in such a diffraction-limited spot. The number of absorbed photons, n_a, per fluorophere and per pulse is [47]:

$$n_a = \frac{P^2\delta}{\tau f}\left(\frac{NA^2}{2\hbar c\lambda}\right)^2 \tag{6.1}$$

where P is the laser power and δ is the fluorophore brightness ($\sigma \cdot \phi_\lambda$) of the fluorophore.

We can compute the number of photons that the chelated indicator absorbs as a function of the laser power, using eq. 6.1. Given the relatively large TPA cross section of FBI (see Methods), $n_a = 2$ for a modest power of 11 mW. Setting the laser power at this value, the emission rate of the chelated molecule will equal the laser repetition rate, $n_f = 1 \times 10^8$ photons/s.

The light emitted by the complexed FBI molecule will be blue-shifted. Assume that a band filter $\lambda_f = (400 - 425)$ nm, is placed in front of the CCD. Call n_f the fluorescence emitted in a given time interval by the chelated indicator. Then, the light recorded by the CCD due to the chelated indicator will be $N_f = \epsilon_f\, \epsilon_c\, n_f$, where $\epsilon_f \sim 0.29$ is the band pass filter efficiency for the signal.

The total fluorescence (green-shifted) emitted by the unchelated molecules will be $m\, n_f / C_r$, and the corresponding background light recorded by the CCD will be $N_b = \epsilon'_f\, \epsilon_c\, m\, n_f / C_r$, where $\epsilon'_f \sim 0.0036$ is the band pass filter efficiency for the background.

The total signal recorded in the CCD will be $N_t = N_f + N_b$. The estimator of the signal observed in the spot will be $N_t - N_b$, where N_b can be computed with great precision taking the average of a large number of spots containing only unchelated molecules. The signal-to-noise ratio (SNR) of the subtraction is:

$$SNR = \frac{N_f}{\sqrt{N_b}} = \sqrt{\epsilon_f \epsilon_c \frac{n_f\, F}{m}} = \sqrt{\frac{7.2 \times 10^{10}}{m}[\mathrm{s}]} \tag{6.2}$$

Notice that SNR is expressed as a function of the time in seconds, since n_f measures number of photons per second. The number of molecules in the diffraction spot will depend on the density of indicators ρ, in the sensor. We assume that the target will be a dense monolayer with about one molecule per square nanometer. As shown by our DFT calculations, the "snowballs" formed by the barium ion during transport (*e.g.*, $Ba^{2+}Xe_8$) will readily form a supra-molecular complex at distances of the order of 1 nm (*e.g.*, 8 Å in the example discussed above). Thus, $\rho = 10^6/\mu m^2$ and $m = 2 \times 10^5$. Substituting in Eq. 6.2 we find SNR $= 6 \times 10^2 \sqrt{\mathrm{s}}$. If we take a scanning time per spot of 1 ms, then SNR$\sim$ 20. Therefore, a chelated indicator would produce an unmistakable signal above the background of unchelated molecules in that spot. This demonstrates that fast and unambiguous identification of Ba^{2+} ions in the sensor can be attained using a dense monolayer. The scanning of large surfaces using wide-field TPA is discussed in Methods.

In summary, we have shown that FBI indicators can be a suitable building block for a sensor able to detect single Ba^{2+} ions in a future HPXe detector, thus allowing an essentially background free experiment.

Figures

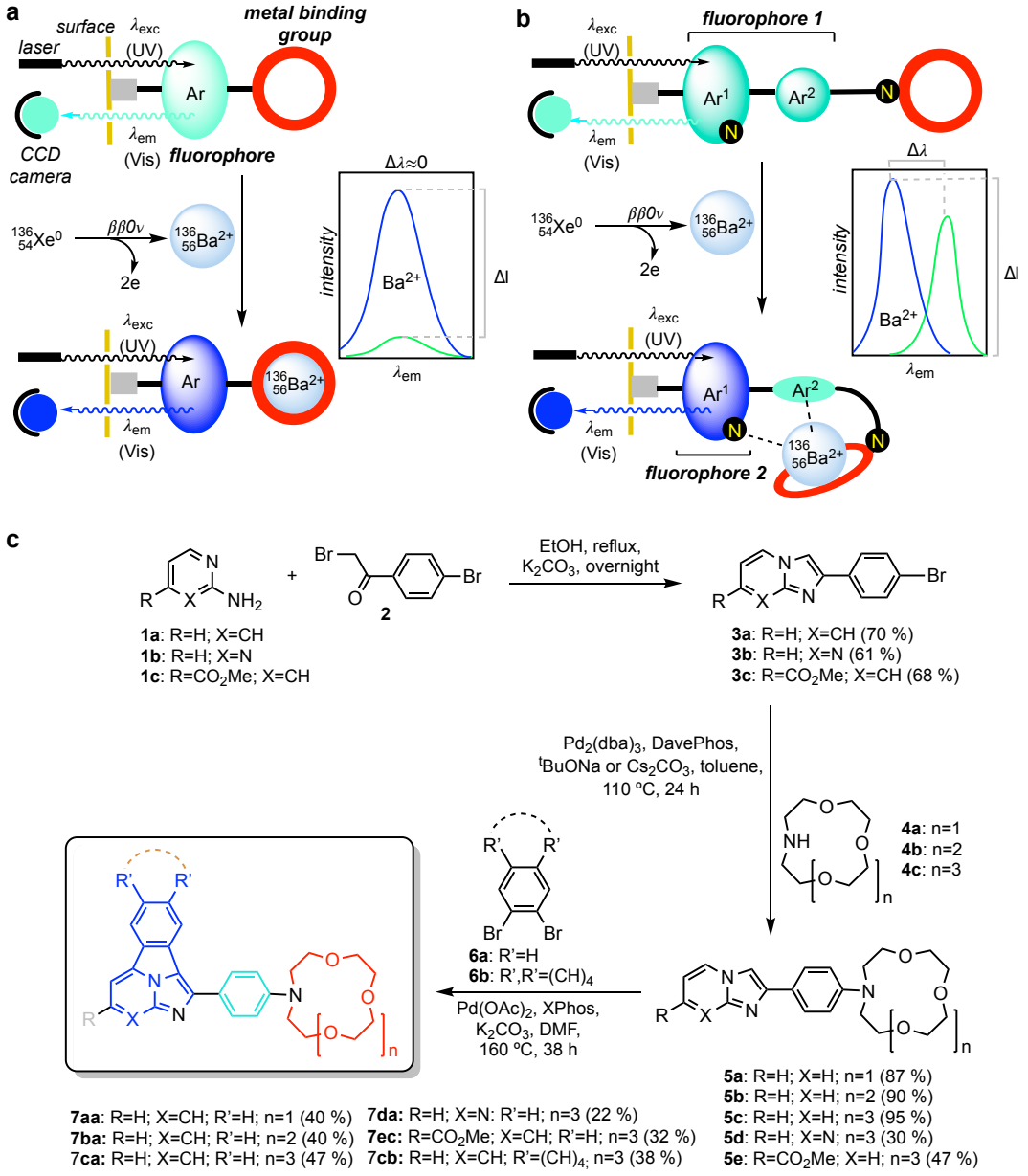

Figure 1. *Design and synthesis of a family of Fluorescent Bicolor Indicators (FBIs).* **a** Components of a Fluorescent Monocolor Indicator (FMI). **b** Components of a FBI analogue, showing the coupling-decoupling between the fluorophore and the metal binding group. The respective expected fluorescent emission spectra are also shown **c**,Chemical synthesis of a family of FBI from pyridines (or pyrimidines), bromoacetophenones, 1,2-dibromoarenes and aza-crown ethers.

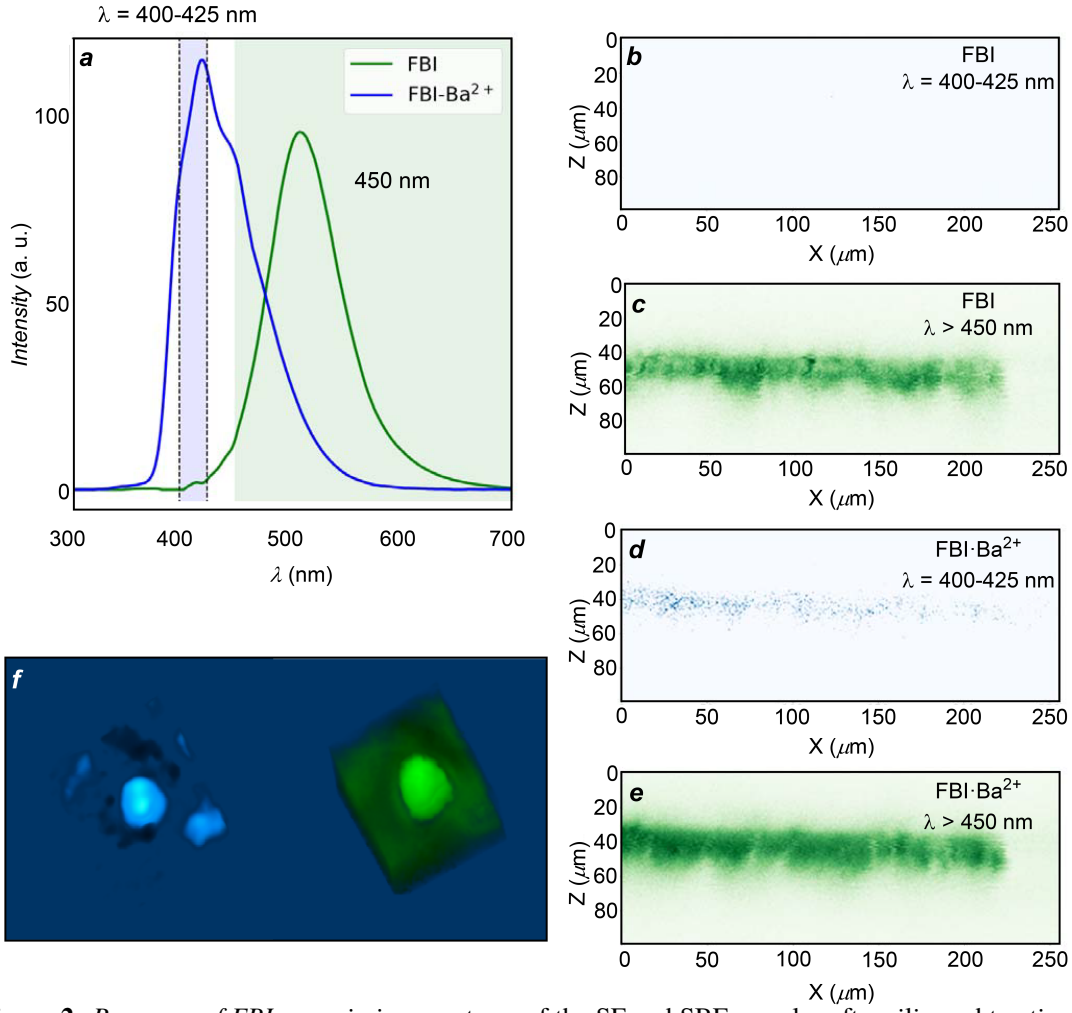

Figure 2. *Response of FBI*. **a**, emission spectrum of the SF and SBF samples after silica subtraction (the SF spectrum is scaled a factor C_r w.r.t. the SBF spectrum); **b**, A Z-X profile of the control pellet, SFpA, showing no signal in the "deep blue" region (400,425) nm, where the contribution from unchelated molecules is negligible; **c**, A Z-X profile of SFpA, taken in the green region ($\lambda > 450$ nm), showing intense green emission from the unchelated molecules ; **d**, A Z-X profile of the sublimated pellet, SFpB, showing a clear signal in the "deep blue" region (400,425) nm, due to the molecules chelated by the barium perchlorate; **e**, A Z-X profile of SFpB, taken in the green region ($\lambda > 450$ nm), showing intense green emission from both chelated and unchelated molecules. **f**, 3D tomographies of SFpB, taken with our TPA microscopy setup, passed through the blue and the green filter. The tomographies reveal the shape of a tiny section (a square of 75 μm size), showing the same landscape for both chelated and unchelated molecules.

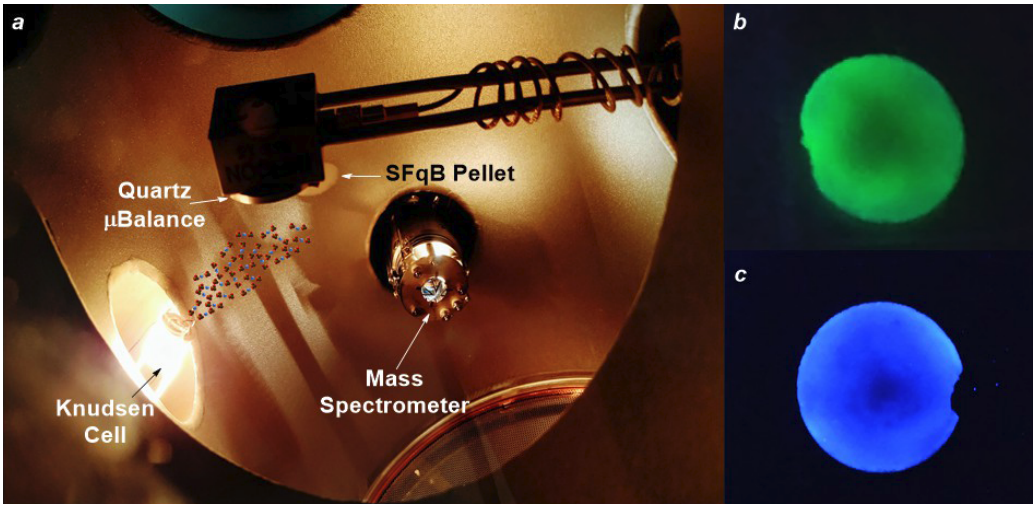

Figure 3. *Sublimation of $Ba(ClO_4)_2$ on FBI*. **a**, experimental setup; **b**, photograph of the pellet before the sublimation and **c**, photograph of the pellet after the sublimation. In both cases, the excitation light is 365 nm. Notice the characteristic green colour of unchelated FBI before the sublimation and the blue shift after it, showing a large density of chelated molecules.

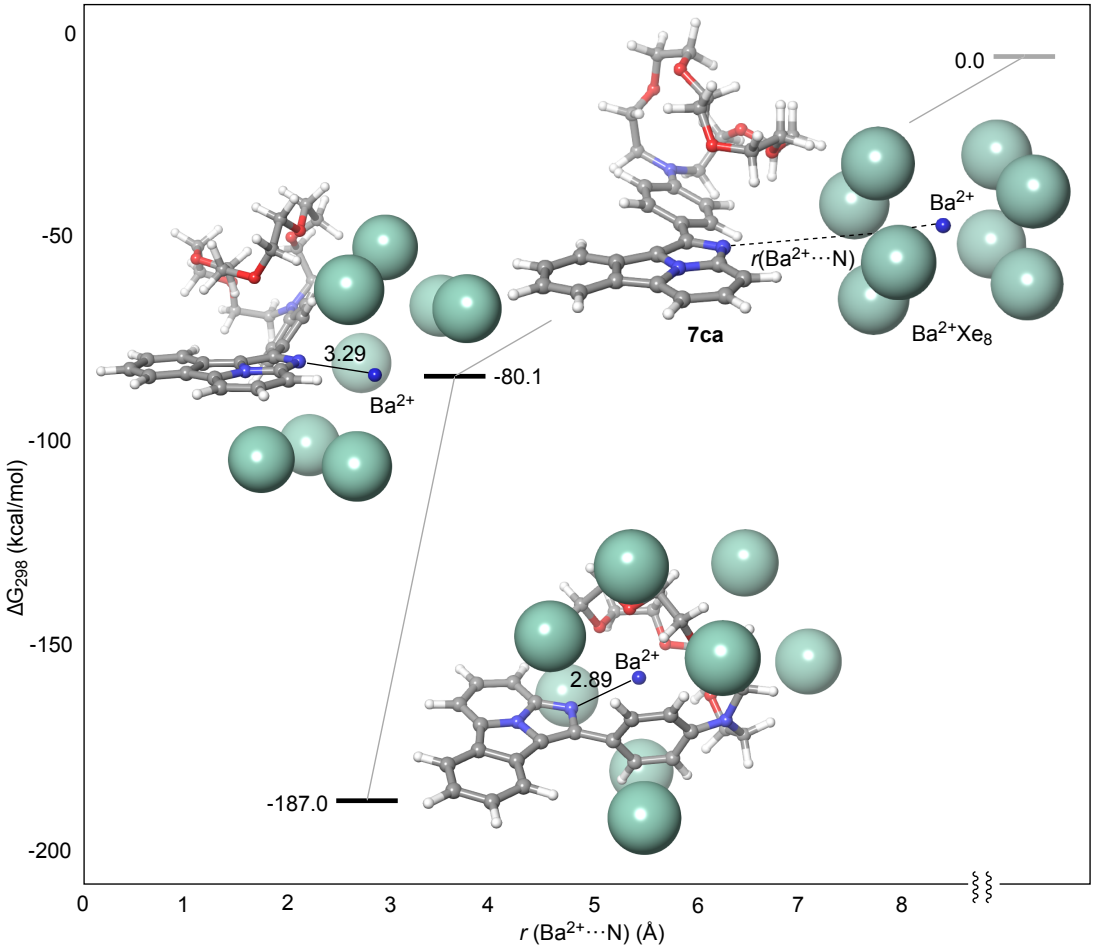

Figure 4. *Computed structures of FBI (**7ca**)and a $Ba^{2+}Xe_8$ cluster at different N···Ba^{2+} distances.* Shown geometries and energies were computed at the ωB97X-D/6-311++G(d,p)&LanL2DZ//B3LYP-D3/6-31G(d)&LanL2DZ level of theory. Xenon atoms are represented in CPK model. The remaining atoms are represented in ball-and-stick model.

7 Methods

Photophysics and supramolecular chemistry of FBI indicators in solution

Our experiments to determine the photo-physical properties of compounds **7** started by recording their respective emission spectra in acetonitrile solutions. Although all compounds were fluorescent with large intensities in the minimum energy transitions, the critical criterion to select the most suitable candidate was the ability of a given compound to exhibit different smallest emission wavelengths in their unbound and barium-coordinated forms. We defined the peak discrimination factor f_λ at a given wavelength λ as:

$$f_\lambda = \frac{I_\lambda(\mathbf{7} \cdot \mathrm{Ba}^{2+}) - I_\lambda(\mathbf{7})}{I_\lambda(\mathbf{7})} \tag{7.1}$$

where $I_\lambda(\mathbf{7}{\cdot}Ba^{2+})$ and $I_\lambda(\mathbf{7})$ are the intensities of the emission signals at wavelength λ of the corresponding bound ($\mathbf{7}{\cdot}Ba^{2+}$) and free (**7**) fluorophore, respectively. In addition, we measured the molecular brightness [48] B_λ of each transition according to the following expression:

$$B_\lambda = \epsilon_\lambda \phi_\lambda \tag{7.2}$$

where ϵ_λ is the molar extinction coefficient and ϕ_λ is the emission quantum yield.

The data associated with the photophysics of compounds **7** are collected in Table 1. According to our results, compound **7aa**, possessing the 1,4,7-trioxa-10-azacyclododecane moiety (**4a**, n=1) does not show any significant difference between the free and barium-bound states, thus indicating that this four-heteroatom aza-crown ether is too small to accommodate the Ba^{2+} cation. Compound **7ba**, with a 1,4,7,10-tetraoxa-13-azacyclopentadecane unit (**4b**, n=2) showed a noticeable blue shift upon coordination with Ba^{2+} ($\Delta\lambda = -54$ nm). However, the low value of f_λ makes this size of the chelating group not optimal for further developments. In the case of FBI molecule **7ca**, which incorporates the six-heteroatom-containing aza-crown ether unit 1,4,7,10,13-pentaoxa-16-azacyclooctadecane (**4c**, n=3), a larger blue shift associated with Ba^{2+} coordination ($\Delta\lambda = -61$ nm) was observed. Most importantly, the f_λ discrimination factor was found to be of order 180, which shows a significant separation between the unbound **7ca** and Ba^{2+}coordinated **7ca**·Ba^{2+} species. Both emission spectra are displayed in Figure A.1. In addition, both unbound and cationic species showed acceptable quantum yields and molecular brightness values.

Having selected compound **7ca** as the best FBI candidate, we conducted studies to assess its binding ability, which must be high (in dry medium) for our sensor. To that end, we measured first its cation association constant K_a with barium perchlorate in acetonitrile at 298 K by means of the Benesi-Hildebrand method [49] and the corresponding fluorescence spectra, according to the following formula [50]:

$$\frac{1}{F - F_{min}} = \frac{1}{F_{max} - F_{min}} \left(1 + \frac{1}{K_a[Ba^{2+}]}\right) \tag{7.3}$$

In this expression, F is the measured emission of compound **7ca** at the excitation wavelength $\lambda_{exc} = 250$ nm in the presence of a given [Ba^{2+}] concentration, whereas F_{min} and F_{max} stand for the corresponding intensities of free aza-crown ether **7ca** and host-guest complex **7ca**·Ba^{2+} respectively.

Under these conditions and on the basis of the data shown in Figure A.1d, we measured a binding constant of $K_a = 5.26\ 10^4\ M^{-1}$ ($r^2 = 0.909$). This indicates a very efficient ability of compound **7ca** for Ba^{2+} capture and formation of the (**7ca**·Ba^{2+})(ClO_4^-)$_2$ salt in solution, whose favourable photophysical parameters are gathered in Table 1. In addition, the Job's plot showed a maximum for $n = m = 1$, thus indicating that **7ca** captures only one Ba^{2+} cation per molecule, as it is shown in Figure A.1e.

As far as the chemical structure of the tetracyclic fluorophore is concerned, our results indicate that introducing an additional nitrogen heteroatom in the 2,2a^1-diazacyclopenta[jk]fluorene to form the corresponding 2,2a^1,3-triazacyclopenta[jk]fluorene analogue is detrimental in terms of quantum yield and molecular brightness, as it can be appreciated from the photophysical properties of compound **7da** shown in Table 1. Moreover, the presence of an additional fused phenyl group in the fluorophore results in the formation of imidazo[5,1,2-cd]naphtho[2,3-a]indolizine derivative **7cb**, whose f_λ factor was significantly lower than that measured for **7ca**. Therefore, the presence of additional fused aromatic or hetheroaromatic rings to the basic benzo[a]imidazo[5,1,2-cd]indolizine scaffold does not improve the photophysical properties of the resulting cycloadduct. Finally, the presence of an electron-withdrawing group in compound **7ec** results in a quenching of quantum yield of the fluorophore as well as a lowering of the discrimination factor. Consequently, we determine that further chemical elaboration of the fluorophore skeleton in order to synthesise the spacer and linker groups shown in Figure 1a, must not involve carboxy derivatives like esters or amides, but π-decoupled moieties such as alkoxy groups. Therefore we conclude that **7ca** is the optimal combination of structural and electronic features to fulfil our previously defined design criteria.

Electronic structure calculations and NMR experiments

Electronic structure calculations at the DFT level both in the gas phase and in solution confirm the strong binding affinity of **7ca** to coordinate Ba^{2+}. The **7ca**·Ba^{2+} optimised structure exhibits a large molecular torsion of the binding group with respect to the free **7ca** molecule (see the ω dihedral angle in Figure A.2b, calculation done at the ωB97X-D/6-311++G(p,d)&Lanl2DZ level of theory), so that a molecular cavity appears, with the metal cation forming a π-complex between the Ba^{2+} metallic centre and the phenyl group. The oxygen atoms of the aza-crown ether occupy five coordination positions with O$\cdots$Ba contacts within the range of the sum of the ionic radii (2.8-3.0 Å) [51]. Interestingly, the phenyl ring attached to the crown ether is oriented towards the centre of the cavity coordinating Ba^{2+} through the π-electrons. Frontier molecular orbitals (MO) of **7ca** are delocalised over the entire fluorophore moiety, with virtually no participation of the binding group electrons (Figure A.2c, computed at the ωB97X-D/6-311G(d,p)/LANDL2DZ level). The lowest bright state of the unbound FBI molecule can be mainly characterised as the electronic transition between highest occupied MO (HOMO) and the lowest unoccupied MO (LUMO). Molecular distortion upon metal coordination in **7ca**·Ba^{2+} has an important impact on the electronic structure. In particular, the torsion of the phenyl group allowing π-coordination breaks the planarity with the rest of the fluorophore, modifying HOMO and LUMO energy levels. The decrease of the effective conjugation with respect to **7ca** increases the symmetry allowed $\pi \rightarrow \pi^*$ gap, thus resulting in the blue shift of the fluorescent emission (Figure A.2c). Therefore, these results support the viability of **7ca** as an efficient Ba^{2+} indicator in both wet and dry conditions (see Supporting Information).

NMR Experiments on the complexation reaction between FIB molecule **7ca** and barium perchlorate are compatible with the geometries obtained by the DFT calculations. Progressive addition of the salt promoted a deshielding to lower field of the *b* protons, which are in *ortho* disposition with respect to the aza-crown ether. The *meta* protons marked as *c* in Figure A.2d showed a similar, but lower in magnitude, deshielding effect. The remaining protons of the benzo[a]imidazo[5,1,2-cd]indolizine fluorophore showed a very light deshielding effect, but remained essentially unchanged. Instead, the 1,4,7,10,13-pentaoxa-16-azacyclooctadecaane moiety of **7ca** showed different deshielding effects upon coordination with Ba^{2+} with the only exception of the *N*-methylene protons denoted as *a* in Figure A.2e, which were shifted to higher field, thus demonstrating that the nitrogen atom of the aza-crown ether is not participating in the coordination with the dication.

7.1 Computed structures of FBI and its complexes with barium perchlorate and barium dication

The optimised molecular geometry of the adduct between FBI (**7ca**) and $Ba(ClO_4)_2$ (Figure A.4) at the DFT level of theory shows a compact structure in which the Ba^{2+} centre does not interact only with the full aza-crown ether but extends its coordination pattern to the N1 atom of the benzo[a]imidazo[5,1,2-cd]indolizine aromatic tetracycle and to the 1,4-disubstituted phenyl group, at the cost of pushing the nitrogen atom N2 of the aza-crown ether away from the closest coordination sphere of Ba^{2+} (compare the $Ba^{2+}\cdots$N1 and $Ba^{2+}\cdots$N2 distances in Table 2). The two perchlorate anions interact with the metallic centre by blocking the extremes of the channel formed by **7ca**, with $Ba^{2+}\cdots$O distances only ca. 0.1 Å larger than those computed for $Ba(ClO_4)_2$. This geometry of the **7ca** $\cdot$ $Ba(ClO_4)_2$ results in the decoupling between the two components of the fluorophore, with a ω value of 45°. The calculated Gibbs energy associated with binding of $Ba(ClO_4)_2$ with FBI is -80.0 kcal/mol. This highly exergonic character is fully compatible with the high binding constant found for this process.

DFT calculations including a naked Ba^{2+} cation bound to **7ca** showed a rigid structure too, in which the main features observed for the **7ca** $\cdot$ $Ba(ClO_4)_2$ complex —namely the interaction of the metallic centre with the N1 atom, the oxygen atoms of the aza-crown ethers and the 1,4-disubstituted aromatic ring— are even more pronounced (Table 2 and Figure A.4). In addition, the free reaction energy associated with this latter process is much more exergonic (ΔG_{rxn}=-197.5 kcal/mol in Table 3). The computed energies exhibit a very small dependency with pressure.

If the formation of clusters between barium cation and xenon atoms is considered, the interaction of a $Ba{\cdot}Xe_8^{2+}$ cluster — a species that can be operative under high-pressure conditions [45] — with FBI results in a still very exergonic process with a Gibbs reaction energy of -195.9 kcal/mol. All these results indicate that the findings obtained in solution for the interaction of FBI compound and barium perchlorate are closely related with the features of the same process in the gas phase involving naked (or Xe-clusterised) barium dications.

Polymer and titration experiments

To measure the response of FBI in dry media, we studied several materials, including silica (which we selected as our preferred support) and three different polymers: polyvinyl alcohol (PVA), polytmethyl metacrylate (PMMA) and poly ether blockamide (PEBAX® 2533).

In the case of silica we conducted a titration experiment, adding increasing concentrations of $Ba(ClO_4)_2$ to the gel before depositing the solution FBI/acetonitrile (in each case measurements were performed in a fluorimeter after drying the solvent). Our results are illustrated in Figure A.4a. We found that the response of the complexed FBI indicator improved with larger concentrations of $Ba(ClO_4)_2$ an effect that we attribute to the affinity of the silica for barium. For the calculation of F presented in this work we chose the largest concentration studied (7927 Eq). Notice, however, that the discrimination factor computed with a concentration of 3964 Eq. (and with concentrations larger than 7927 Eq. not shown in plot) yields a very similar result, compatible with the error quoted for F.

Our results for the studies with polymers are summarised in Figure A.4b, which shows the response of the indicator in PMMA. Under excitation light of 350 nm, the spectra of both chelated and unchelated molecules are rather similar and cannot be effectively separated. All the other polymers exhibit a similar behaviour. We attribute the lack of separation between the spectra of chelated and unchelated indicators to the restriction of the conformational freedom imposed by the polymer's rigid environment.

Subtraction of the silica response

Figure A.5 shows the response of the silica to and excitation light of 250 nm. Notice that the subtraction of the silica response results in a zero baseline (and a significant subtraction error) for wavelengths below $\sim$ 370 nm. Above that value the chelated spectrum raises quickly, while the unchelated spectrum raises only above $\sim$ 400 nm. The separation between both spectra is very large in the region (370-400) nm, where the response of the uncomplexed spectrum is compatible with zero, but the systematic error in the measurement of the discrimination factor is also large (40%). In the selected region (400, 425) nm, the separation is still large and the systematic error is reduced to 20%.

Laser setup

A schematic diagram of our laser setup is depicted in Figure A.6a. We took advantage of the fact that the emission spectra of FBI and FBI·Ba^{2+} for excitation light of 250 nm and excitation light of 400 nm are very similar (Figure A.6b), to use a mode-locked Ti:Sapphire infrared laser (800 nm) as illumination source, inducing the absorption of two photons of 400 nm each. This laser system provided pulses of infrared light with a repetition rate of 76 MHz. The pulse duration was 400 fs at the sample's plane.The beam was reflected at a dichroic mirror, passed a non-immersion objective (20x, A=0.5) and reached the sample, illuminating a spot limited by diffraction to a volume of about 1 μm^3. A DC-motor coupled to the objective allowed optical sectioning across the sample along the Z-direction. This image modality is known as XZ tomographic imaging. We call *profiles* to those tomographic images (similar to the B scanning mode used in optical coherence tomography clinical devices). In addition, we performed 3D tomographies, which were assembled from 40 XY scans of 75 $\mu m^2 \times 75\ \mu m^2$. Each scan corresponded to a different depth of Z, in steps of 10 µm. The resulting images were then combined in a 3D image using custom software [44]. The emitted light was collected through the same objective and passed the dichroic mirror. Finally, before reaching the photomultiplier tube used as detection unit, the TPA signal passed through either a high pass "green" filter, $\lambda > 450$ nm, or a band pass "deep blue" filter, (400 – 425) nm.

In order to estimate the absolute number of fluorescence photons emitted by the FBI indicator in a TPA scan, we first measured a reference sample of fluorescein suspended in PVA (FRS). Figure A.6c shows a log-log plot of the recorded PMT signal as a function of the laser power for FRS. As expected for TPA, the slope of the resulting straight line has a value near 2. Figure A.6d, shows a profile taken on FRS at a power of 80 mW. Identical profiles were taken on SBFp at a power of 40 mW. This allowed the measurement of the ratio $\delta_r = \delta_{sbfp}/\delta_{frs}$, which turned out to be $\delta_r = 17 \pm 4$, and therefore, $\delta_{FBI\cdot Ba^{2+}} = 6.2 \pm 1.7 \times 10^2$ GM. The details of the measurement are discussed below.

Determination of the brightness of FBI relative to fluorescein

The fluorophore brightness ($\delta = \sigma \cdot \phi_\lambda$, where σ is the TPA cross section and ϕ_λ the quantum yield) of fluorescein is well known for a wavelength of 800 nm [52]: $\delta_{fluo} = 36 \pm 9.7$ GM (1 GM= 10^{-50} cm^4·second/ (photon·molecule)). It is, therefore, possible to normalise the brightness of FBI to that of fluorescein, using samples of known concentrations and measuring the response in our setup for identical profiles. To that end, we used a control sample of fluorescein suspended in PVA (FPVA), with a concentration of $n_{fpva} = 10^{13}$ molecules/cm^3 and compared it with a FBI-chelated pellet (SBFp), which had a concentration of $n_{sbfp} = 2.2 \times 10^{17}$ molecules/cm^3. Profiles were taken on FPVA at a power of 500 mW. Identical profiles were taken on SBFp at a power of 100 mW. The total signal integrated by the PMT in both the FPVA and SBFp samples is:

$$I = K \cdot n \cdot \delta \cdot P^2 \tag{7.4}$$

where n is the density of molecules (molecules/cm^3) in the sample and P is the laser power. K is a constant which depends of the setup, but is the same for the FPVA and SBFp profiles. It follows that:

$$R_{fbi/fluo} = \frac{\delta_{sbfp}}{\delta_{fpva}} = \frac{I_{sbfp}}{I_{fpva}} \frac{n_{fpva}}{n_{sbfp}} \left(\frac{P_{fpva}}{P_{sbfp}}\right)^2 \tag{7.5}$$

All the quantities in equation 7.5 are known. In particular, the integral of the SBFp profile yields 10^9 PMT counts, while the integral of the FPVA profile results in 5.9×10^4 counts. Thus, we find : $R_{fluo/fbi} = 17 \pm 4$, where the $\sim 20\%$ relative error is dominated by the uncertainty in the concentration n_{sbfp}, and therefore, $\delta_{FBI\cdot Ba^{2+}} = 6.2 \pm 1.2 \times 10^2$ GM.

Interaction of FBI with other elements

The interaction of FBI (**7ca**) with other elements was studied in order to assess the selectivity of the indicator. In particular, we chose several dications within the alkaline-earth elements to which barium belongs, as well as sodium and potassium, which are found abundantly in the environment and occupy contiguous positions in the alkaline group of the periodic table. Solutions (5×10^{-5} M) of **7ca** and metal source in ratio 1:1 were prepared for this study. We used $Ca(OH)_2$, $K(ClO_4)$, $Na(ClO_4)$, $Mg(ClO_4)_2$, $Sr(ClO_4)_2$ and $Ba(ClO_4)_2$ with CH_3CN as a solvent. The results are summarised in Figure A.7. We observed that Mg^{2+} induced a partial intensity lowering (ON-OFF) effect) at the same emission wavelength upon interaction with **7ca**, whereas Ca^{2+} did not produce any noticeable change in its fluorescence emission spectrum when mixed with **7ca**. Therefore, we concluded that our indicator does not produce significant changes in the emission wavelength in the presence of light

alkaline-earth dications. In contrast, in the presence of **7ca** Sr^{2+} exhibited an emission espctrum similar to that observed for Ba^2+. These results show that **7ca** is capable to chelate Sr^{2+} and Ba^{2+}. It is therefore expected that **7ca** should chelate Ra^{2+}. Finally, according our results, neither K^+, nor Na^+ were chelated by **7ca**, thus evidencing the high selectivity of our indicator.

A BOLD concept

We conceive the Barium atOm Light Detector (BOLD) as an HPXe TPC implementing a full Barium Tagging Detector (BTD). The concept presented here extends the ideas presented in [19, 23, 24] (other possibilities that could apply to a future HPXe with barium tagging are discussed in [53]). BOLD consists in three major systems. An Energy-Tracking Detector (ETD), whose role is measuring the energy and t_0 of the event, as well as reconstructing its topology (and in particular its barycentre), and a Barium Tagging Detector (BTD), capable of tagging, with high efficiency, the single Ba^{2+} ion produced in a $\beta\beta0\nu$ or $\beta\beta2\nu$ decay. The information of these two systems is linked through the Delayed Coincidence Trigger (DCT), whose role is to establish a coincidence between the observation of the two-electron signal, and the detection of Ba^{2+}. The DCT is essential to eliminate the impact of $\beta\beta2\nu$ events, which also produce Ba^{2+} but whose energy is always outside of the region of interest (ROI) for $\beta\beta0\nu$ events. The DCT also supresses radioactive processes to virtually zero. Notice that the individual probabilities that spurious events produce two electrons with energy within the ROI and a positive signal in the BCT are very small, but the probability that those events occur at the same time (in fact with a known delay) is essentially negligible.

Figure A.8 shows a cartoon of BOLD. A future, ton-scale appparatus may be quite large, *e.g.*, $2.5\,m^3 \times 2.5\,m^3 \times 2.5\,m^3$, holding a mass of near 3 t at (very) high pressure (40 bar). Conceptually, the detector is as follows: The ETD is a dense array of large silicon photomultipliers (SiPMs), located behind the transparent anode which is connected to high voltage. The BTD is located behind the grounded cathode and deploys an array of sensors called Molecular Target Elements (MTE) assembled in a low-mass honeycomb also connected to voltage and normally held at a slightly positive value. Each MTE is a tile, made of Muscovite mica, of $2.5\,cm^2 \times 2.5\,cm^2$ transverse dimensions and 0.5 mm thickness. A self-assembled monolayer (SAM) of FBI indicators is grown in one of the sides of the tile, and placed facing the TPC fiducial volume. About 10^4 tiles cover a detection surface of $2.5\,m^2 \times 2.5\,m^2$. The MTEs are interrogated by a fast TPA laser microscopy system (TPAL), consisting in one or more pressure-resistant objectives, able to move, on demand, to the specific area of the BTD which needs to be scanned. The laser will be a high-power (2-3 MW), pulsed, femto-second, 100 MHz (or 1 GHz) system, entering the chamber through suitable windows, and steered by piezo-electric actuated mirrors. A prototype of such a system is already under development as a part of the NEXT R&D [53].

The delayed coincidence trigger is activated by the ETD, when the energy of the event is measured to be within the ROI signalling an event of interest (recall that the energy of $\beta\beta0\nu$ events is Q). When this happens, the ETD reconstructs the barycentre of the event and computes the time of arrival of the Ba^{2+} to the BTD (relying in the time difference between the recording of primary and secondary electroluminescence signals, a standard technique for electroluminescent TPCs [54]). It then sends the coincidence trigger which lowers the voltage of the BTD (normally held at ~ 100 V, so that all positive ions are absorbed by the cathode) to some -100 V, during a time window large enough (about 1 ms) to allow that the putative Ba^{2+} ion arriving to the cathode can “cross the gate”,

reach the BTD and be captured by one of the MTEs. The predicted arrival position of the ion is also known from the barycentre of the event and sent to the TPAL, which scans it. After scanning, the TPAL sends a signal if a chelated molecule has been found. The signature of a $\beta\beta0\nu$ event is the **coincidence** between the energy trigger, the time trigger opening the cathode gate, and the TPAL positive trigger.

To determine the precision in the prediction of the transverse position of the arrival ion we have written a Monte Carlo simulation, based in the Geant-4 package [55], that takes into account the essential features of the detector (ionisation of the primary media, diffusion of the ionisation electrons and response of the sensors). We obtain that the barycenter of the event can be determined, at a pressure of 40 bar with an error (1 σ) of 5 mm, while the time of arrival can be determined from the sampling time of the electronics with an error better than 100 µs. Therefore, the Ba^{2+} candidate will be contained in a scanning region of 1.5 cm^2 × 1.5 cm^2 more than 99% of the times.

In order to scan such an area in a reasonable time, is necessary to implement large field-of-view (FOV) techniques. For example, a FOV of 100 µm diameter, and an interrogation rate of 1 ms per FOV, result in a scanning time of 13 s/cm^2, which allows the scanning of the barium-fiducial area (1.5 cm^2 × 1.5 cm^2) in ∼30 s.

Indeed, the availability of lasers with peak powers of several watts, makes fast scanning possible using wide-field two-photon microscopy [56]. If, instead of focusing into a diffraction limited spot by overfilling the back aperture of the objective (as discussed in the example given in the main body of the paper), we choose to focus into a small spot near the back aperture, a wider (and weaker) spot at the target plane is produced. The number of absorbed photons in this configuration, decreases with $(r/r_d)^2$, where r is the wide-field radius and r_d the radius of the diffraction limit spot. Taking r =50 µm and r_d =0.5 µm, we find that $n_a^{wf} = n_a\ 10^{-4}$, where n_a^{wf} is the number of absorbed photons in the wide-field configuration. However, these four orders of magnitude can be accounted for thanks to the P^2 dependence of n_a. Indeed, we find that $n_a^{wf} = 2$ for a power of 2.1 watt. Projecting each diffraction-limited spot in the FOV in one CCD pixel is then possible to find if any pixel in the CCD has a chelated molecule with high SNR (∼ 20) in 1 ms, (the last generation of CCD cameras features speeds in excess of 1000 frames per second), and thus fast scanning is feasible.

The Ba^{2+} will slowly drift to the cathode (with a drift velocity of about 220 cm s^{-1}) picking up neutral xenon atoms in its way, so that a variety of solvation states, $[BaXe_N]^{2+}$ (with $N = 1, 2...$) will be formed [45]. At the large pressures relevant for BOLD, $N \sim 8$. However, as shown in this paper, the Gibbs energy of all the solvation states is similar and very large. Given the favourable energy balance, the probability of forming a supra-molecular complex will likely be close to unity.

The fraction of $\beta\beta0\nu$ events in the ROI for a detector with 0.7% FWHM resolution, as envisioned for BOLD [11] (The NEXT-White detector has achieved already 1% FWHM energy resolution [57]) can be estimated to be [58]:

$$F_{\beta\beta2\nu} = \frac{c}{Q\delta^6} m_e \tag{7.6}$$

where $\delta = \Delta E/Q$ is the FWHM energy resolution, m_e is the electron mass and $c = 8.5$ for $\delta \sim 1\%$. For a FWHM of 0.7% and $Q = 2458$ keV in xenon, we find that $F_{\beta\beta2\nu} \sim 5 \times 10^{-9}$. The SNR between the $\beta\beta0\nu$ and the $\beta\beta2\nu$ processes is found multiplying by the ratio of the lifetimes:

$$\frac{S}{B} = \frac{1}{F} T_{1/2}^{2\nu} T_{1/2}^{0\nu} \tag{7.7}$$

Taking $T_{1/2}^{2\nu} = 2.1 \times 10^{21}$ [59], we find that $S/B \sim 10$ for $T_{1/2}^{0\nu} = 5 \times 10^{28}$.

Consequently, the $\beta\beta2\nu$ background is negligible in the foreseeable range of lifetimes to be explored, provided that the detector has good resolution, as is our case. Notice that, by setting the DCT to trigger only in events within the ROI, the Ba^{2+} produced by $\beta\beta2\nu$ events never reach the BCT, since the cathode gate will be closed. Thus, "contamination" of Ba^{2+} from $\beta\beta2\nu$ events can be controlled to negligible levels. In practice, $\beta\beta2\nu$ events will be used to calibrate the system and measure the Ba^{2+} detection efficiency. Notice that the detector area will be $\sim 2.5 \times 10^9$ spots of $100\,\mu m^2 \times 100\,\mu m^2$, and thus one can afford "expending" $\sim 10^5$ spots per year (in calibration events), resulting in less than 0.1% losses in efficiency after 10 years. Also notice that the location within a MTE of each calibration event would be recorded by the system, avoiding any potential confusion with a genuine signal.

The scanning methodology deserves also some comments. During fabrication of the BTD each of the MTEs will be scanned and a map of pixels will be recorded. The map will contain the position of the pixel and the intensity response in the "deep blue band" (*e.g.*, a filter (400 – 425) nm) to the interrogation of the scanning laser operating at the nominal parameters. The initial scan will allow to identify and reject defective MTEs and veto any potential defective spots.

In normal operations, when the DCT triggers the scan of a specific region, the system records the signal in each spots and compares it with the reference in the data base, as well as with the running average computed on the fly. This allows us to take into account any local variation of density in the MTEs, as well as fluctuations in the laser power which are, in any case controlled with very good precision. The systematic error that we obtain simulating these parameters is small compared with the bulk effect of the subtraction of the light due to unchelated molecules. Setting a very high nominal SNR (20 in our analysis) also provides extra protection against spurious fluctuations, which in our analysis never yielded SNR larger than 3. To conclude, we believe that a robust and reliable TPA scanning system can be implemented allowing high efficiency and virtually zero background for Ba^{2+} detection.

A Extended data figures and tables

Cmpd.	a		b	c		d	
	$\lambda_{em}(nm)$		f_λ	Φ_λ		$B_\lambda(M^{-1}cm^{-1})$	
	7	**7**·Ba^{2+}	**7**·Ba^{2+}	**7**	**7**·Ba^{2+}	**7**	**7**·Ba^{2+}
7aa	485	485	0.07	0.42	0.41	8.42	8.45
7ba	482	428	6.02	0.34	0.32	7.65	8.13
7ca	489	428	179.74	0.67	0.45	11.26	8.06
7da	491	491	n. d.	0.06	0.06	0.53	0.51
7ec	511	430	22.64	0.29	0.25	3.65	3.05
7cb	503	456	4.86	0.22	0.04	4.84	1.21

Table 1. Characterisation of FBI compounds **7** and **7**·Ba^{2+}. **a**, Emission wavelengths at an excitation wavelength of 250 nm. **b**, Peak discrimination factors, f_λ, with respect to unbound fluorophores **7** at λ_{em}. **c**, Quantum yields, Φ_λ, at λ_{em}. **d**, Molecular brightnesses of the fluorescent emissions, B_λ, at λ_{em}; n. d.: not determined.

7ac·Ba^{2+}	ωB97X-D	B3LYP-D3
Ba^{2+}-O_1	2.84	2.87
Ba^{2+}-N_1	2.92	2.94
Ba^{2+}-N_2	3.82	3.91
Ba^{2+}-X	3.03	3.04
ω	82.9	76.3
7ac·$Ba(ClO_4)_2$	ωB97X-D	B3LYP-D3
Ba^{2+}-O_1	2.84	2.85
Ba^{2+}-O_2	2.79	2.90
Ba^{2+}-O_3	2.94	2.96
Ba^{2+}-N_1	3.04	3.14
Ba^{2+}-N_2	4.15	4.53
Ba^{2+}-X	3.20	3.59
ω	45.0	43.1

Table 2. Structural parameters for the geometries of **7ac**·Ba^{2+} and **7ac**·$Ba(ClO_4)_2$ optimised in vacuum at the DFT level wit two different functionals and basis set: ωb97X-D/6-311++G(d,p)&LanL2DZ and B3LYP-D3/6-31G(d)&LanL2DZ. Bond distances and dihedral angles (in absolute value) are given in Å and degrees, respectively. Atomic labels are shown in Figure A.3.

reaction	pressure (atm)	ΔG_{rxn} (kcal/mol)
7ca + Ba^{2+} → **7ac**·Ba^{2+}	1	-197.5
	10	-198.8
	20	-199.2
	30	-199.5
7ca + Ba·Xe_8^{2+} → **7ca**·Ba^{2+} + 8Xe	1	-195.9[a]
7ca + $Ba(ClO_4)_2$ → **7ac**·$Ba(ClO_4)_2$	1	-80.0

[a]Free energy computed as the sum of FBI and eight individual Xe atoms.

Table 3. Free energy of reactions calculated as $\Delta G_{rxn} = \sum G_{prod} - \sum G_{react}$ at T = 298.15 K computed at the ωb97X-D/6-311++G(d,p)&LanL2DZ level.

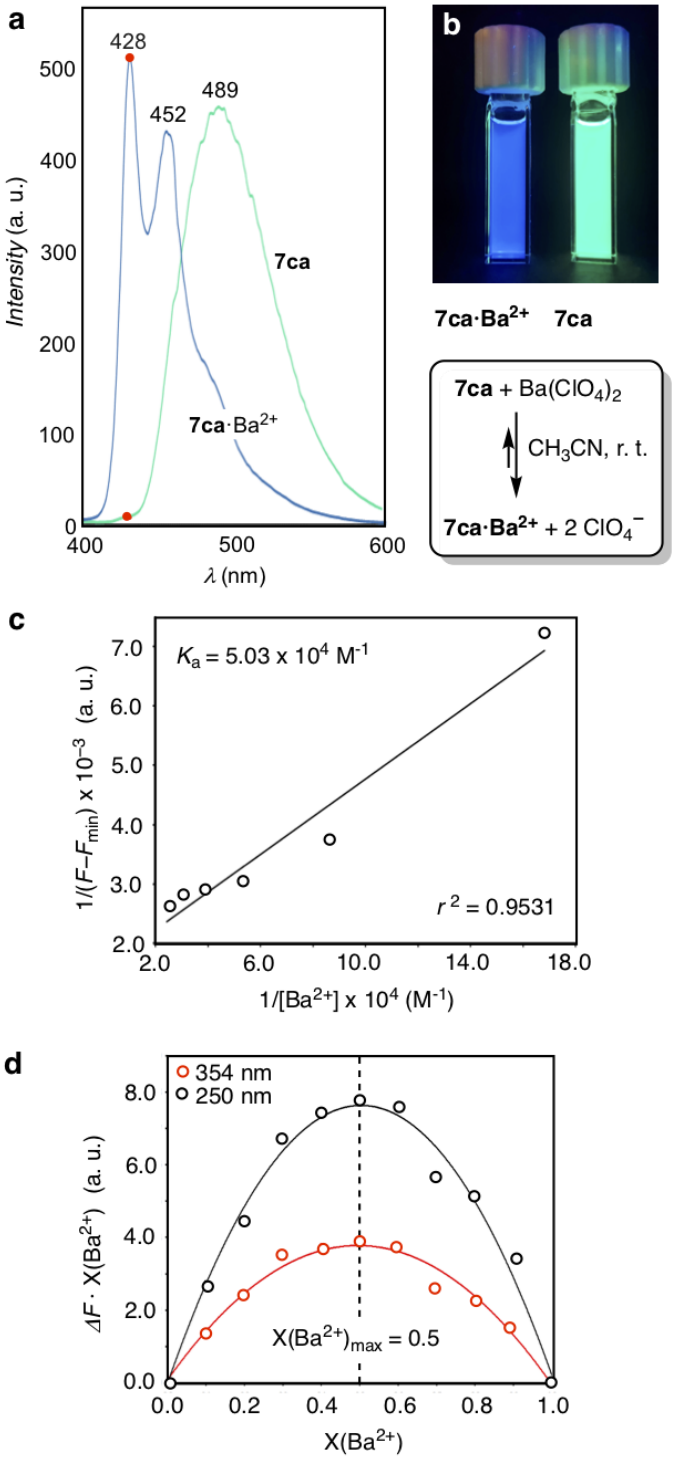

Figure A.1. *Characterisation of FBI in solution.* **a**, Emission spectra of unchelated (**7ca**) and chelated (**7ca**·Ba^{2+}) indicators upon excitation at 250 nm. Red dots indicate the wavelengths used to determine the peak discrimination factor f_λ. **b**, Photographs of both species in acetonitrile showing the bicolor emission, upon irradiation at 365 nm. **c**, Benesi-Hildebrand plot of the fluorescence emission spectra of FBI in acetonitrile solution at room temperature in the presence of different concentrations of barium perchlorate. **e**, Job's plot of the **7ca**-$Ba(ClO_4)_2$ interaction showing a 1:1 stoichiometry between **7ca** and Ba^{2+} thus forming complex **7ca**·Ba^{2+}.

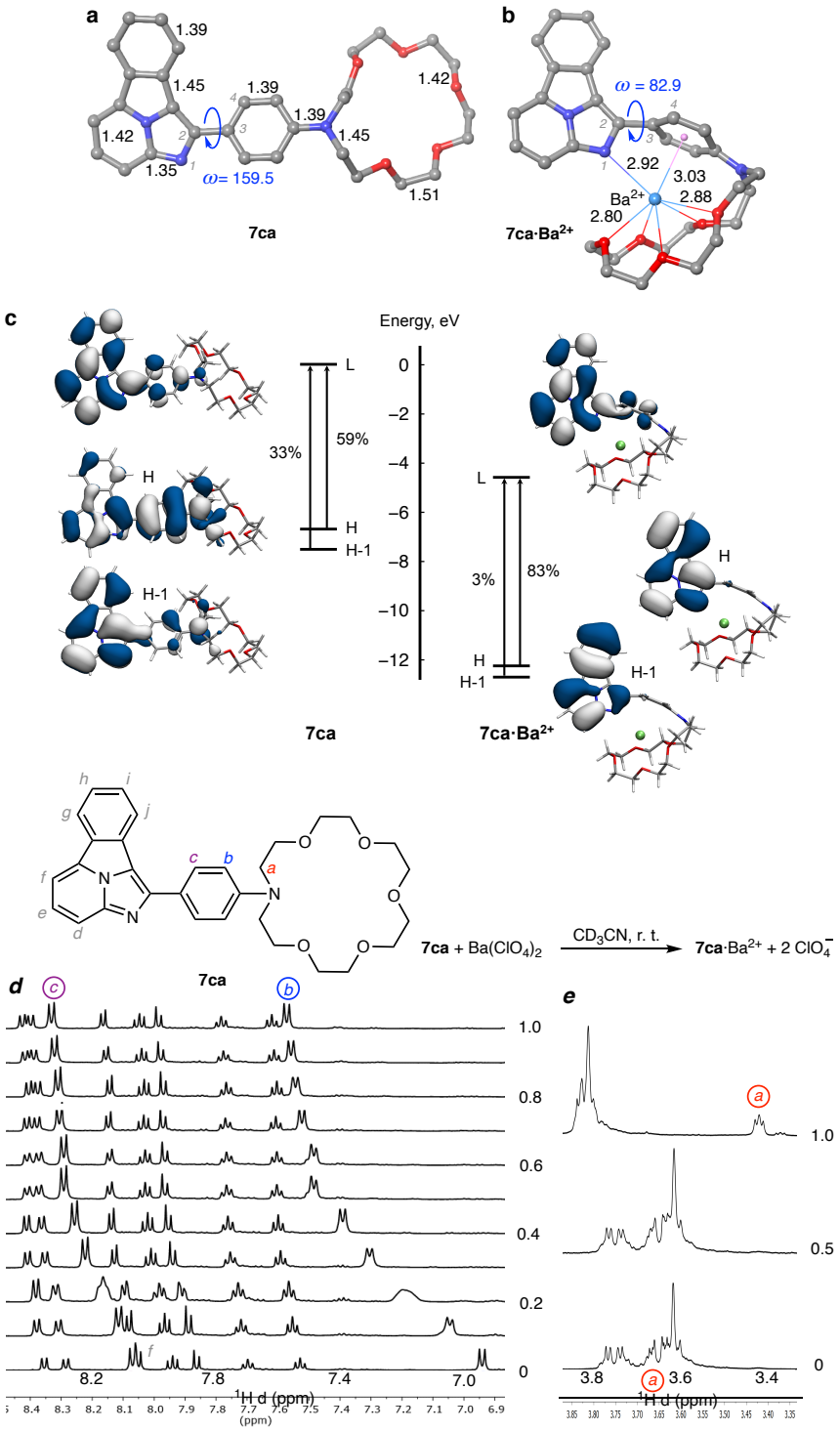

Figure A.2. *Theoretical predictions and NMR experiments*. Top panel: Density functional theory gas phase structures of **a**, **7ca** and **b**, **7ca**· Ba^{2+}. Bond distances are given in Å. Dihedral angles ω formed by covalently bonded atoms 1-4 are given in deg and in absolute value. **c**, Frontier molecular orbital energy diagram of **7ca** (left) and **7ca**· Ba^{2+}(right). Vertical arrows indicate main contributions to the electronic transition to the lowest bright state. Bottom panel: Aromatic **d**, and aza-crown ether **e**, regions of proton NMR spectra of compound **7ca** upon addition of barium perchlorate. The most important changes in chemical shift (in ppm) are highlighted. All the spectra were recorded at 500 MHz.

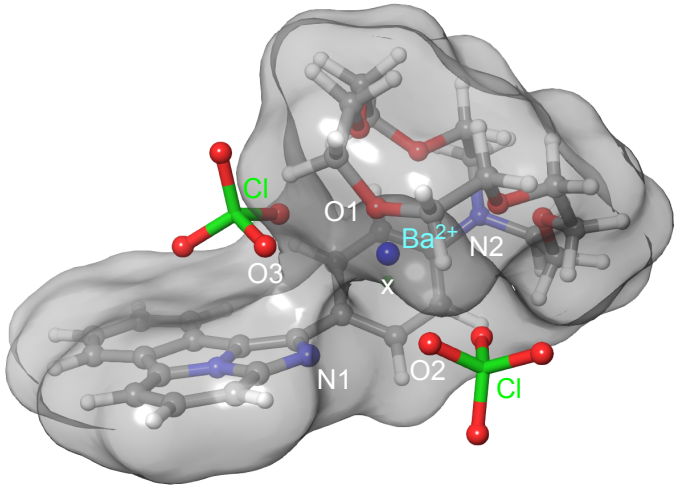

Figure A.3. *Computed structures of FBI-barium perchlorate complex*. DFT fully optimised structure of **7ca** complexed with barium perchlorate. Dummy atom located at the centre of the 1,4-disubstituted phenyl group is denoted as **X**. Bond distances and dihedral angles are given in Table 2.

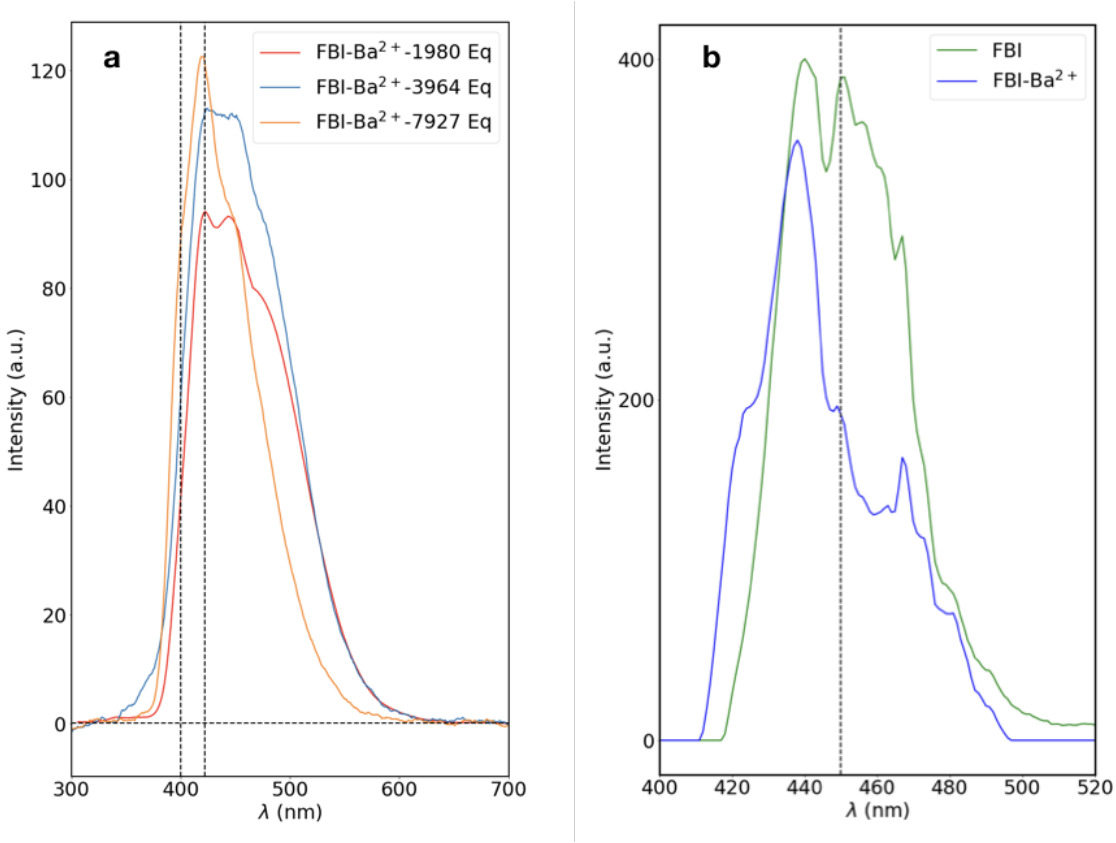

Figure A.4. *Titration and polymer experiments*. **a**, titration experiments, showing that the response of FBI improves for larger concentrations of barium; **b**, an example of a polymer experiment, showing that the response of FBI loses its characteristic colour shift.

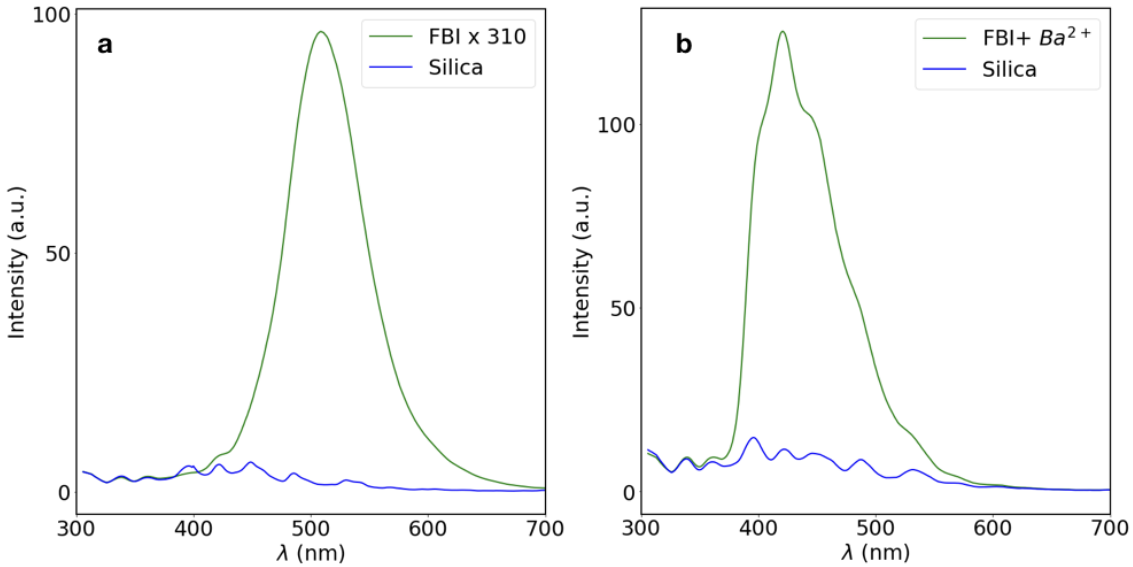

Figure A.5. *Subtraction of the silica response*. **a**, emission spectrum of the SF sample with the background from the silica superimposed for an excitation light of 250 nm; **b**, same for SBF.

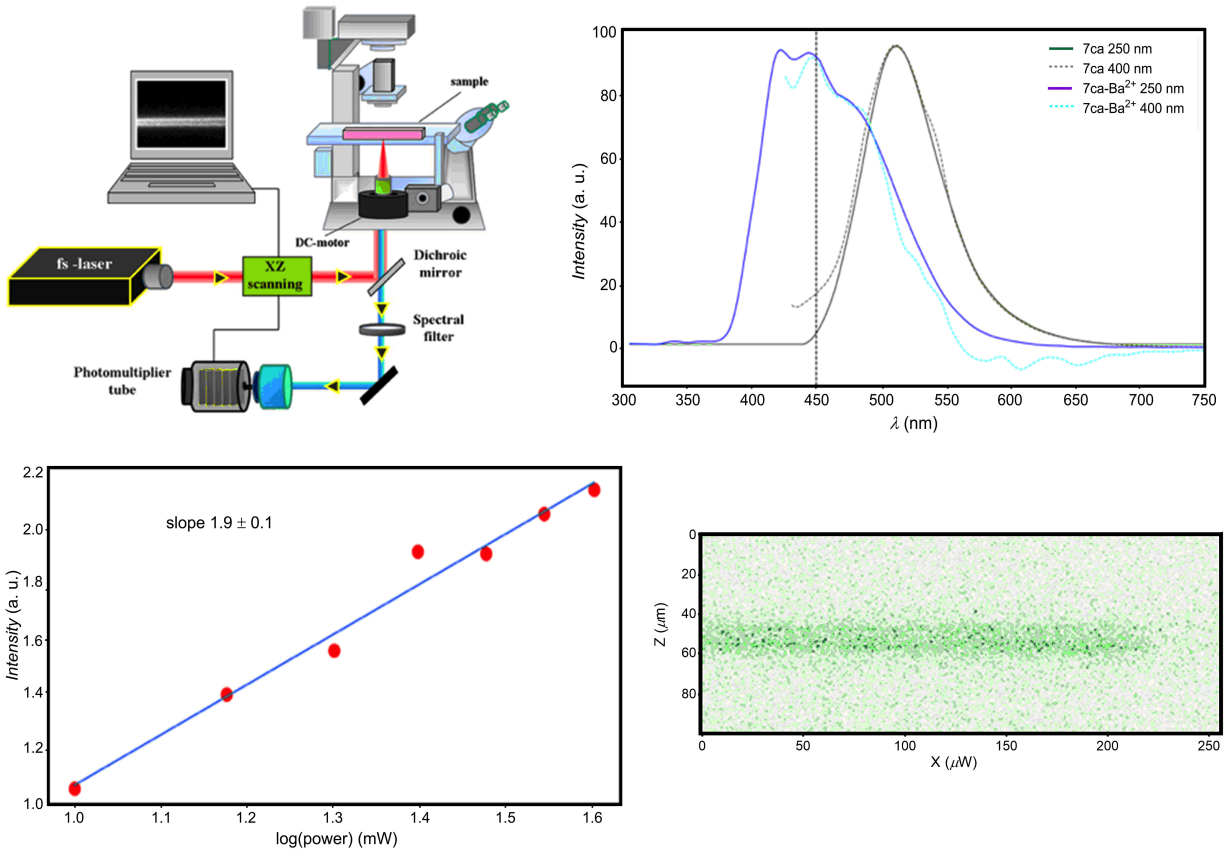

Figure A.6. *TPA microscopy*. **a**, A cartoon of our setup. An infrared (800 nm) laser passes through a dichroic and fills the back plane of the objective (20x NA = 0.5) of an inverted microscope. The laser is focused in the sample, with a spot limited by diffraction (*e.g.* a volume of about 1 μm^3). The emitted fluorescence passes through a selection filter before being recorded by a photomultiplier. **b**, Emission spectra of FBI and FBI·Ba^{2+} for excitation light of 250 nm (green, blue) and an excitation light of 400 nm (olive, cyan). The spectra are very similar, allowing the use of an infrared laser of 800 nm for our proof-of-concept. **c**, Log-log plot showing the quadratic dependence of the intensity with the power, characteristic of TPA, for a fluorescein reference sample (FRS). **d**, Two-dimensional scan (profile) across the FRS. Integration of the profile yields and integrated signal which can be used as normalisation for the FBI samples.

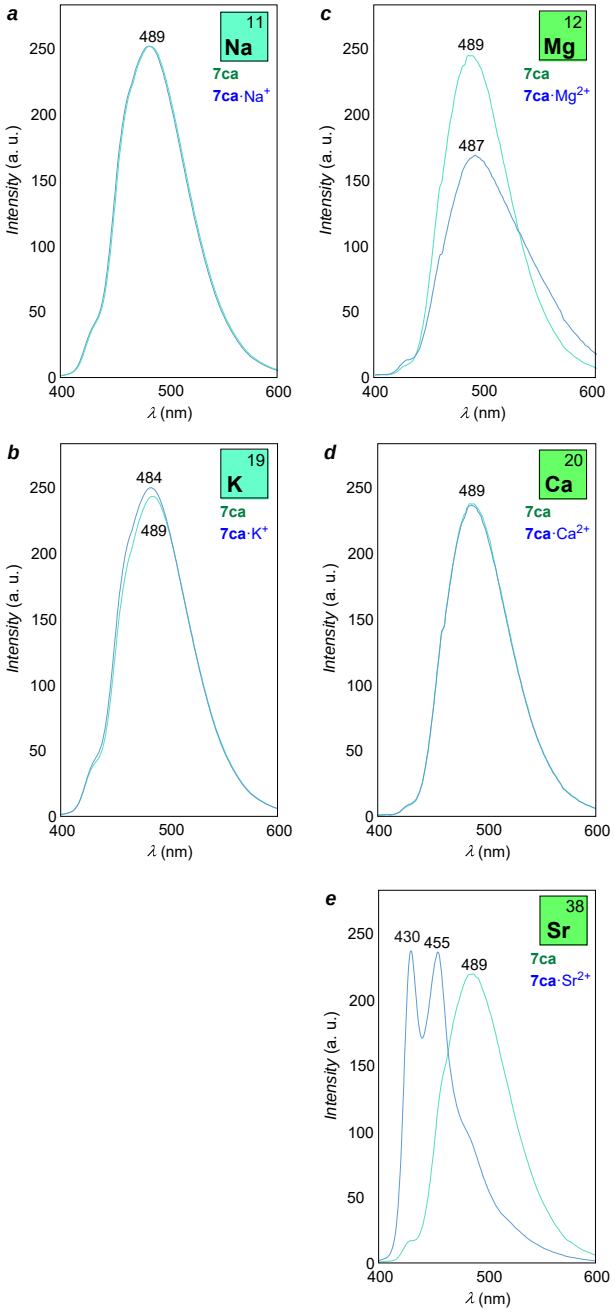

Figure A.7. *Interaction of FIB with other elements (1:1 equiv.).* **a**, FIB·Na^+ (blue) and unchelated (green) indicators. **b**, FIB·K^+ (blue) and unchelated indicators. **c**, FIB·Mg^{2+} (blue) and unchelated (green) indicators. **d**, FIB·Ca2+ (blue) and unchelated (green) indicators. **e**, FIB·Sr^{2+} (blue) and unchelated (green) indicators. In cases of a, b, c and d, the spectra show that FIB is not chelated with the ion, while in case e, the response is similar to barium, showing the formation of a supramolecular complex. All excitation spectra taken at 250 nm.

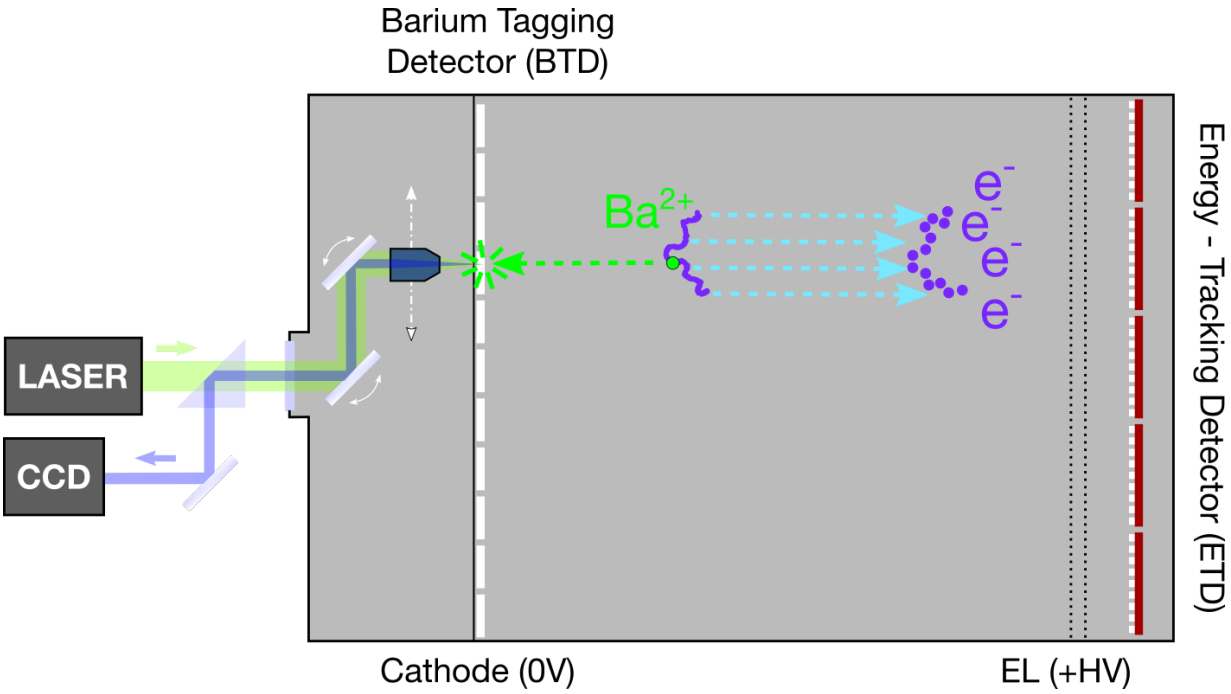

Figure A.8. A scheme of the BOLD detector. An example of a $\beta\beta0\nu$ signal event is shown. The two electrons emitted in the decay (purple) propagate in the dense xenon gas ionising it, and the ionisation electrons drift towards the anode, where their energy is measured by the Energy Tracking Detector (ETD), which also reconstructs the event barycentre. The Ba^{2+} ion drifts much slowly towards the cathode, where it is eventually captured and identified by the Barium Tagging Detector (BTD).

Acknowledgments

We acknowledge the support of our colleagues of the NEXT collaboration in the development of this work as a part of the R&D program to to develop a background-free experiment based in Ba^{2+} tagging. We also acknowledge support from the following agencies and institutions: the European Research Council (ERC) under the Advanced Grant 339787-NEXT; the Ministry of Science, Universities and Research of Spain and FEDER under grants FIS2014-53371-C04, FIS2016-76163-R, MAT2016-78293-C6-5-R, MINECO/FEDER CT2016-80955-P, CTQ2016-80375-P and CTQ2014-51912-REDC; Interreg POCTEFA V-A Spain–France–Andorra Program (EFA 194/16/TNSI); the Basque Government (GV/EJ, grant IT-324-07 and IT1180-19). Agencia de Ciencia y Tecnología de la Región de Murcia (19897/GERM/15). The authors also thank the SGI/IZO-SGIker UPV/EHU, Fundación Séneca and the DIPC for generous allocation of computational and analytical resources.

Author contributions. J.J.G.C., F.P.C. and D.N. conceived the project. J.J.G.C. and F.P.C. coordinated the experiments and analysed the data. I.R. and B.A. carried out the chemical synthesis, characterisation and solution fluorescence studies of the compounds. J.I.M. carried out the NMR experiments. C.T., F.P.C. and D.C. performed the computational studies. P.H. and C.R designed and performed the chelation in dry medium. Z.F. carried out the fluorescence studies in silica experiments. B.O. and T.S. performed the solid phase experiments involving polymers. J.M.B., R.M.M., P.H., F.M. and P.A., performed the laser experiments (coordinated by J.M.B). J.J.G.C. and F.P.C. wrote the manuscript. D.N., F.M., C.R. and P.A. assisted in writing and editing the manuscript.

Competing interests. The authors declare no competing interests.

References

[1] Gómez Cadenas, J. J., Martín-Albo, J., Mezzetto, M., Monrabal, F. & Sorel, M. The Search for Neutrinoless Double Beta Decay. *Riv. Nuovo Cim* **35**, 29–98 (2012).

[2] Majorana, E. Theory of the Symmetry of Electrons and Positrons. *Nuovo Cim.* **14**, 171–184 (1937).

[3] Sakharov, A. D. Violation of cp invariance, c asymmetry, and baryon asymmetry of the universe. *Pisma Zh.Eksp.Teor.Fiz. 5 32-35* (1967).

[4] Fukugita, M. & Yanagida, T. Baryogenesis Without Grand Unification. *Phys. Lett.* **B174**, 45–47 (1986).

[5] Gell-Mann, M., Ramond, P. & Slansky, R. Complex Spinors and Unified Theories. *Conf. Proc.* **C790927**, 315–321 (1979). 1306.4669.

[6] Yanagida, T. Horizontal gauge symmetry and masses of neutrinos. *Conf. Proc.* **C7902131**, 95–99 (1979).

[7] Mohapatra, R. N. & Senjanovic, G. Neutrino Mass and Spontaneous Parity Nonconservation. *Phys. Rev. Lett.* **44**, 912 (1980). [,231(1979)].

[8] Gando, A. *et al.* Search for Majorana Neutrinos Near the Inverted Mass Hierarchy Region with KamLAND-Zen . *Phys. Rev. Lett.* **117**, 109903 (2016). URL https://link.aps.org/doi/10.1103/PhysRevLett.117.109903.

[9] Agostini, M. *et al.* Improved Limit on Neutrinoless Double-β Decay of ^{76}Ge from GERDA Phase II. *Phys. Rev. Lett.* **120**, 132503 (2018). arXiv.1803.11100.

[10] Alduino, C. *et al.* First Results from CUORE: A Search for Lepton Number Violation via $0\nu\beta\beta$ Decay of ^{130}Te. *Phys. Rev. Lett.* **120**, 132501 (2018). arXiv.1710.07988.

[11] Gomez-Cadenas, J. J. Status and prospects of the NEXT experiment for neutrinoless double beta decay searches (2019). arXiv.1906.01743.

[12] Moe, M. K. New approach to the detection of neutrinoless double beta decay. *Physical Review* **C44**, 931–934 (1991).

[13] Danilov, M. *et al.* Detection of very small neutrino masses in double beta decay using laser tagging. *Physics Letters* **B480**, 12–18 (2000). hep-ex/0002003.

[14] Sinclair, D. *et al.* Prospects for Barium Tagging in Gaseous Xenon. *Journal of Physics Conference Series* **309**, 012005 (2011).

[15] Mong, B. *et al.* Spectroscopy of Ba and Ba^+ deposits in solid xenon for barium tagging in nEXO. *Physical Review* **A91**, 022505 (2015). arXiv.1410.2624.

[16] Chambers, C. *et al.* Imaging individual barium atoms in solid xenon for barium tagging in nEXO. *Nature* **569**, 203–207 (2019). arXiv.1806.10694.

[17] Albert, J. B. *et al.* Measurements of the ion fraction and mobility of alpha- and beta-decay products in liquid xenon using the exo-200 detector. *Phys. Rev. C* **92**, 045504 (2015). URL http://link.aps.org/doi/10.1103/PhysRevC.92.045504.

[18] Bolotnikov, A. & Ramsey, B. The spectroscopic properties of high-pressure xenon. *Nuclear Instruments and Methods in Physics Research A* **396**, 360–370 (1997).

[19] Nygren, D. R. Detecting the barium daughter in136xe 0-$\nu\beta\beta$ decay using single-molecule fluorescence imaging techniques. *Journal of Physics: Conference Series* **650**, 012002 (2015).

[20] Nygren, D. High-pressure xenon gas electroluminescent TPC for $0-\nu\,\beta\beta$-decay search. *Nucl.Instrum.Meth.* **A603**, 337–348 (2009).

[21] Álvarez, V. *et al.* NEXT-100 Technical Design Report (TDR): Executive Summary. *JINST* **7**, T06001 (2012). arXiv.1202.0721.

[22] Martín-Albo, J. *et al.* Sensitivity of NEXT-100 to Neutrinoless Double Beta Decay. *JHEP* **05**, 159 (2016). arXiv.1511.09246.

[23] Jones, B. J. P., McDonald, A. D. & Nygren, D. R. Single Molecule Fluorescence Imaging as a Technique for Barium Tagging in Neutrinoless Double Beta Decay. *JINST* **11**, P12011 (2016). arXiv.1609.04019.

[24] McDonald, A. D. *et al.* Demonstration of Single Barium Ion Sensitivity for Neutrinoless Double Beta Decay using Single Molecule Fluorescence Imaging. *Phys. Rev. Lett.* **120**, 132504 (2018). arXiv.1711.04782.

[25] Thapa, P. *et al.* Barium Chemosensors with Dry-Phase Fluorescence for Neutrinoless Double Beta Decay. *Sci. Rep.* **9**, 15097 (2019). 1904.05901.

[26] Ji, H.-F., Dabestani, R., Brown, G. M. & Hettich, R. Spacer length effect on the photoinduced electron transfer fluorescent probe for alkali metal ions. *Photchem. Photobiol. 69, 513-516.* (1999).

[27] Nakahara, Y., Kida, T., Nakatsuji, Y. & Akashi, M. Fluorometric sensing of alkali metal and alkaline earth metalcations by novel photosensitive monoazacryptand derivatives in aqueous micellar solutions. *Org. Biomol. Chem. 3, 1787-1794.* (2005).

[28] Bissell, R. A. *et al.* Luminescence and charge transfer. part 2. aminomethyl anthracene derivatives as fluorescent pet (photoinduced electron transfer) sensors for protons. *J. Chem. Soc. Perkin Trans. 2 . 1559-1564.* (1992).

[29] Bourson, J., Pouget, J. & Valeur, B. Ion-responsive fluorescent compounds. 4. effect of cation binding on the photophysical properties of a coumarin linked to monoaza- and diaza-crown ethers. *J. Phys. Chem. 97, 4552-4557.* (1993).

[30] Li, J., Yim, D., Jang, W.-D. & Yoon, J. Recent progress in the design and applications of fluorescence probes containing crown ethers. *Chem. Soc. Rev. 46, 2437-2458.* (2017).

[31] Valeur, B. & Berberan-Santos, M. N. Molecular fluorescence —principles and applications. *(Wiley–VCH, Verlag & Co. KGaA, 2012) 420-436* .

[32] Huston, M. E., Haider, K. W. & Czarnik, A. W. Chelation enhanced fluorescence in 9,10-bis[[(2-(dimethylamino)ethyl)methylamino]methyl]anthracene. *J. Am. Chem. Soc. 110, 4460-4462.* (1988).

[33] Carter, K. P., Young, A. M. & Palmer, A. E. Fluorescent sensors for measuring metal ions in living systems. *Chem. Rev. 114(8) 4564-4601* (2014).

[34] Golchini, K. *et al.* Synthesis and characterization of a new fluorescent probe for measuring potassium. *Am. J. Physiol. 258(2), F438-F443* (1990).

[35] Yang, J.-S., Hwang, C.-Y., Hsieh, C.-C. & Chiou, S.-Y. Spectroscopic correlations between supermolecules and molecules. anatomy of the ion-modulated electronic properties of the nitrogen donor in monoazacrown-derived intrinsic fluoroionophores. *J. Org. Chem. 69, 719-726.* (2004).

[36] Smith, G. A. & Hesketh, J. C., T. R.and Metcalfe. Design and properties of a fluorescent indicator of intracellular free sodium concentration. *Biochem. J. 250(1), 227-232.* (1988).

[37] Crossley, R., Goolamali, Z. & Sammes, P. G. Synthesis and properties of a potential extracellular fluorescent probe for potassium. *J. Chem. Soc. Perkin Trans. 2 (7), 1615-1623.* (1994).

[38] Aginagalde, M. *et al.* Tandem [8 + 2] cycloaddition-[2 + 6 + 2] dehydrogenation reactions involving imidazo[1,2-a]pyridines and imidazo[1,2-a]pyrimidines. *J. Org. Chem., 75 (9), 2776-2784* (2010).

[39] Zhang, Y., Tang, S., Thapaliya, E. R., Sansalone, L. & Raymo, F. M. Fluorescence activation with switchable oxazines. *Chem. Commun. (Cambridge, U. K.), 54 (64), 8799-8809.* (2018).

[40] Ko, C.-C. & Yam, V. W.-W. Coordination compounds with photochromic ligands: Ready tunability and visible light-sensitized photochromism. *Acc. Chem. Res. , 51 (1), 149-159* (2018).

[41] Maitra, R., Chen, J.-H., Hu, C.-H. & Lee, H. M. Synthesis and optical properties of push-push-pull chromophores based on imidazo[5,1,2-cd]indolizines and naphtho[1',2':4,5]imidazo[1,2-a]pyridines. *Eur. J. Org. Chem. (40), 5975-5985* (2017).

[42] Dougherty, D. A. The cation-π interaction. . (2013).

[43] Ávila, F. J., Gambín, A., P., A. & M., B. J. In vivo two-photon microscopy of the human eye. *Sci. Reports 9, 10121* (2019).

[44] Bueno, J. *et al.* Multiphoton microscopy of ex vivo corneas after collagen cross-linking. *Investigative Ophthalmology & Visual Science, Vol. 52, No. 8* (2011).

[45] Bainglass, E., Jones, B. J. P., Foss, F. W., Huda, M. N. & Nygren, D. R. Mobility and Clustering of Barium Ions and Dications in High Pressure Xenon Gas. *Phys. Rev.* **A97**, 062509 (2018). arXiv.1804.01169.

[46] Zinter, J. P. & Levene, M. J. Maximizing fluorescence collection efficiency in multiphoton micros. *OSA Vol. 19, No. 16 / OPTICS EXPRESS 15348* (2011).

[47] W Denk, W. W., JH Strickler. Two-photon laser scanning fluorescence microscopy. *Science, Vol. 248, Issue 4951, pp. 73-76 DOI: 10.1126/science.2321027* (990).

[48] Carter, K. P., Young, A. M. & Palmer, A. E. Fluorescent sensors for measuring metal ions in living systems. *Chem. Rev. (Washington, DC, U. S.) 114 (8), 4564-4601.* (2014).

[49] Benesi, H. A. & Hildebrand, J. H. A spectrophotometric investigation of the interaction of iodine with aromatic hydrocarbons. *J. Am. Chem. Soc., 71, 2703–2707* (1949).

[50] Zhang, Q. & Duan, K. Fluorescence chemosensor containing 4-methyl-7-coumarinyloxy, acetylhydrazono and n-phenylaza-15-crown-5 moieties for k+ and ba2+ ions. *Heterocycl. Commun., 24 (3), 141–145* (2018).

[51] Batsanov, S. S. Van der waals radii of elements. *Inorganic Materials, 37 (9), 871–895* (2001).

[52] Xu, C. & Webb, W. W. Measurement of two-photon excitation cross sections of molecular fluorophores with data from 690 to 1050 nm. *J. Opt. Soc. Am. B 481* (1995).

[53] Byrnes, N. K. *et al.* Barium Tagging with Selective, Dry-Functional, Single Molecule Sensitive On-Off Fluorophores for the NEXT Experiment. In *Meeting of the Division of Particles and Fields of the American Physical Society (DPF2019) Boston, Massachusetts, July 29-August 2, 2019* (2019). 1909.04677.

[54] Monrabal, F. *et al.* The Next White (NEW) Detector. *JINST* **13**, P12010 (2018). 1804.02409.

[55] Agostinelli, S. *et al.* Geant4 - a simulation toolkit. *Nucl. Instrum. Meth. A 506, 250-303* (2003).

[56] R, A. *et al.* Widefield two-photon excitation without scanning: Live cell microscopy with high time resolution and low photo-bleaching. *PLoS ONE 11(1): e0147115. doi:10.1371/journal.pone.0147115* (2016).

[57] Renner, J. *et al.* Energy calibration of the NEXT-White detector with 1% resolution near $Q_{\beta\beta}$ of ^{136}Xe. *JHEP* **10**, 230 (2019). 1905.13110.

[58] Elliott, S. R. & Vogel, P. Double beta decay. *Ann. Rev. Nucl. Part. Sci.* **52**, 115–151 (2002). hep-ph/0202264.

[59] Ackerman, N. *et al.* Observation of Two-Neutrino Double-Beta Decay in Xe-136 with EXO-200. *Phys. Rev. Lett.* **107**, 212501 (2011). 1108.4193.